
MULTI-VIEW POLARIMETRIC SCATTERING CLOUD TOMOGRAPHY AND RETRIEVAL OF DROPLET SIZE

PREPRINT

Aviad Levis*

Viterbi Faculty of Electrical Engineering
Technion - Israel Institute of Technology
Haifa, 3200003, Israel
aviad.levis@gmail.com

Yoav Y. Schechner

Viterbi Faculty of Electrical Engineering
Technion - Israel Institute of Technology
Haifa, 3200003, Israel
yoav@ee.technion.ac.il

Anthony B. Davis

Jet Propulsion Laboratory
California Institute of Technology
Pasadena, CA, 91109
Anthony.B.Davis@jpl.nasa.gov

Jesse Loveridge

Dept. of Atmospheric Sciences
University of Illinois
Champaign, IL, 61820
jesser12@illinois.edu

May 26, 2020

ABSTRACT

Tomography aims to recover a three-dimensional (3D) density map of a medium or an object. In medical imaging, it is extensively used for diagnostics via X-ray computed tomography (CT). Optical diffusion tomography is an alternative to X-ray CT that uses multiply scattered light to deliver coarse density maps for soft tissues. We define and derive tomography of cloud droplet distributions via passive remote sensing. We use multi-view polarimetric images to fit a 3D polarized radiative transfer (RT) forward model. Our motivation is 3D volumetric probing of vertically-developed convectively-driven clouds that are ill-served by current methods in operational passive remote sensing. These techniques are based on strictly 1D RT modeling and applied to a single cloudy pixel, where cloud geometry is assumed to be that of a plane-parallel slab. Incident unpolarized sunlight, once scattered by cloud-droplets, changes its polarization state according to droplet size. Therefore, polarimetric measurements in the rainbow and glory angular regions can be used to infer the droplet size distribution. This work defines and derives a framework for a full 3D tomography of cloud droplets for both their mass concentration in space and their distribution across a range of sizes. This 3D retrieval of key microphysical properties is made tractable by our novel approach that involves a restructuring and differentiation of an open-source polarized 3D RT code to accommodate a special two-step optimization technique. Physically-realistic synthetic clouds are used to demonstrate the methodology with rigorous uncertainty quantification.

Keywords Polarization, 3D Radiative Transfer, Inverse Problems, Tomography, Remote Sensing, Convective Clouds, Cloud Microphysics

1 Introduction & Outline

Clouds play a significant role at local and global scales, affecting weather, the water cycle, solar power generation, and impacting Earth's energy balance [1]. Moreover, uncertainties in global climate models are significantly affected by our limited understanding, and therefore modeling, of cloud dynamics and microphysics [2]. Thus, understanding, modeling, and predicting cloud properties is a key issue with worldwide socio-economic implications that is in the

*Now at the Computing and Mathematical Sciences Department, California Institute of Technology, Pasadena, CA, 91125.

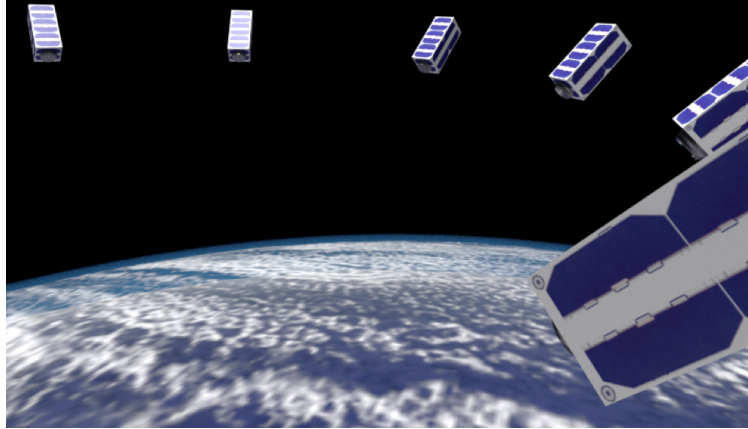


Figure 1: Artist’s illustration of the CloudCT [8] mission: a distributed multi-view system of 10 nano-satellites orbiting the Earth in formation. Measurements acquired by the formation will enable tomographic retrievals of cloud properties.

center of many research studies [3]. Much of the current understanding relies on routine remote sensing of cloud properties such as by the MODerate resolution Imaging Spectrometer (MODIS) [4]. In practice, global-scale retrievals have so far been based on an individual pixel basis, using a crude approximation that clouds are plane-parallel slabs. This approximation uses a 1D radiative transfer (RT) model, which leads to biases in many retrievals [5] while other retrievals simply fail [6]. Convective clouds are therefore a blind spot due to their 3D nature.² In its 2018 *Decadal Strategy for Earth Observation from Space* [7], the National Academies of Sciences, Engineering, and Medicine have indeed identified “Clouds, Convection, and Precipitation” as one of its five top-priority Targeted Variables for NASA’s next generation of satellite missions. To bridge this gap, new technology is needed to study clouds as 3D volumetric objects, on a global scale. The *CloudCT* [8] space mission, by the European Research Council (ERC) is specifically destined to provide data and products for this goal. It will involve 10 nano-satellites orbiting in formation, thus acquiring simultaneously unique multi-view measurements of such vertically-developed 3D clouds (Fig. 1).

Moreover, common retrieval of cloud droplet characteristics use two optical bands simultaneously [9]: a visible band, where reflected radiance increases with cloud optical thickness, and a shortwave IR (SWIR) band, where absorption by condensed water depends on cloud droplet size. To sense droplet size in 3D by CloudCT or other future missions, sensors will need to have either SWIR or polarization capability.

1.1 Why polarized light?

There is an additional caveat in common retrievals, which rely on SWIR absorption [9]. In addition to absorption, light undergoes multiple scattering in clouds. Multiple scattering diminishes sensitivity to droplet microphysics. High sensitivity to microphysics is embedded in single-scattering events. It is thus beneficial to pick-up single-scatter signals, out of the strong multiply-scattered background radiance. Polarization signals of scattered light are dominated by single-scattering events, and are thus highly sensitive to the type and size specifications of scatters. Thus in recent years, there is growing interest in polarimetric imagers for remote sensing of clouds and aerosols [10, 11, 12, 13, 14, 15]. In turn, increased interest in polarimetric sensing capabilities has led to the development of 1D and 3D polarized (or “vector”) RT codes [16, 17] with an aim of improving retrieval algorithms. Motivated by the CloudCT mission formulation—only the first of many to come in innovative passive cloud remote sensing—we develop herein a novel framework for 3D remote sensing of cloud properties using multi-view polarimetric measurements.

1.2 Why passive tomography?

From its etymology, the word “tomography” means a slice-by-slice recovery of an object’s 3D internal structure using 2D projections of cumulative density. In the computer age, this task is termed *Computed Tomography* (CT) [18]. Common medical CT approaches are transmission-based X-ray CT or single-photon emission computed tomography (SPECT). There, 2D projections represent straight line-of-sight (LOS) integrals of the local X-ray opacity or nuclear marker density, respectively. In both imaging modalities, the inverse problem of recovering the medium content is *linear* [19].

² Shallow convective clouds in the planetary boundary layer are also overlooked due to their unresolved scale in low-resolution sensors.

Biomedical imaging also involves CT modalities which are not based on linear projections. A prime example is Optical Diffusion Tomography (ODT) [20, 21, 22], which uses non-ionizing near-infrared light. It is worth noting the work by Che et al. [23] which departs from physics-based approaches into the realm of machine-learning.

In ODT, a patient’s organ is surrounded by a large number of point sources of pulsed isotropic near-infrared irradiation and a large number of time-resolving omnidirectional sensors. The organ transmits radiation diffusely, with very little absorption. Anomalous 3D absorbing or vacuous regions can be detected and assayed using *nonlinear* inverse diffusion spatiotemporal analysis, that relies on very high orders of scattering. The detected radiance is blurred, yielding limited 3D spatial resolution. However, ODT can yield sufficient diagnostic information, using non-ionising radiation.

Medical CT modalities generally use *active* radiation. Active methods are also used for *local* atmospheric sensing or scatterers by radar and lidar. There, a transmitter and receiver are generally collocated and signals are based on backscattering and time-resolved two-way transmission. Probing is solved per LOS using methods which are computationally relatively simple. However, the technology is expensive, horizontal sampling is generally very limited, and irradiance decays fast from the transmitter. Passive sensing is less expensive, uses minimal power, and can image wide swaths of Earth. Thus *global coverage mandates passive imaging from space*. Consequently, this paper focuses on derivation of 3D passive tomography of scatterer fields.

Passive remote sensing does not benefit from pulsed sources for echo-location. It should rely on multi-angular data. Linear CT models (analogous to medical Xray CT and SPECT) were used to study gas emission and absorption in 3D plumes in the vicinity of pollution sources [24, 25] or volcanoes [26, 27]. There, Rayleigh-scattered sunlight was transmitted through the gas to a spectrometer on a platform flying around the plume. Following the vision of Werner et al. [28], Huang et al. [29, 30] used scanning microwave radiometers to reconstruct 2D slices of particle density in clouds based on its impact on local emissivity.

Linear CT was also adapted by Garay et al. [31] to characterize a smoke plume over water emanating from a coastal wild fire. There, the signal is sunlight scattered to space and detected by the Multi-angle Imaging Spectro-Radiometer (MISR) sensor [32] at nine viewing angles. The analysis in [31] yields the direct transmission through the plume per LOS, from which linear CT analysis yields the plume density without using solar radiometers under the plume.

In general, however, retrieving atmospheric scatterer fields in 3D requires a full forward model of scattering in 3D. The model satisfies neither a direct transmission model of linear CT, nor the diffusion limit of ODT. In passive imaging of scatterers, the light source irradiating the atmosphere is the sun: uncontrolled, steady and mono-directional. Aides et al. [33] formulated CT based on single-scattered light. Their forward model is based on sets of broken-ray paths, where light changes direction once from the sun to a sensor.

All the above atmospheric tomography methods assumed the medium to be optically thin enough for direct and once-scattered radiation to dominate the measured radiance. We depart radically from this assumption, drawing inspiration from the success of active ODT, though necessarily with a different forward model. We formulate an inverse 3D RT problem for cloud tomography utilizing multi-view multi-spectral polarimetric images. In contrast to linear CT, the image formation model is nonlinear in the microphysical and density variables. Our approach seeks an optimal fit of droplet microphysical parameters. This is based on a computational 3D polarized RT forward model, the *vector Spherical Harmonics Discrete Ordinates Method* (vSHDOM) [34, 35]. To this effect, we generalize our demonstrated iterative inversion approach [36, 37, 38] to take advantage of polarimetric measurements.

1.3 Outline

In the next section, we cover basic cloud droplet optics using Mie scattering theory and the fundamentals of polarized 3D RT. The latter yields radiance which has a clear decomposition into single- and multiply-scattered light. This decomposition supports the solution to the inverse problem at hand. We then lay out our 3D cloud tomography method where we target three basic microphysical properties, volumetrically. Necessary but tedious mathematical details are presented in the *Appendix*. Subsequently, the new 3D cloud tomographic capability is demonstrated on realistic synthetic clouds from a Large Eddy Simulation (LES) that provide ground truth for unambiguous retrieval error quantification. We conclude with a summary of our results and an outline of future developments, mostly looking toward CloudCT and other future space-based uses.

2 Background

This section describes bulk microphysical parameterization of scattering media, the polarimetric radiative transfer image formation (forward) model and the relation between them. The section also describes the coordinate systems in use (per-scatterer, imager and Earth frames). We further decompose the polarized radiance into single-scattered

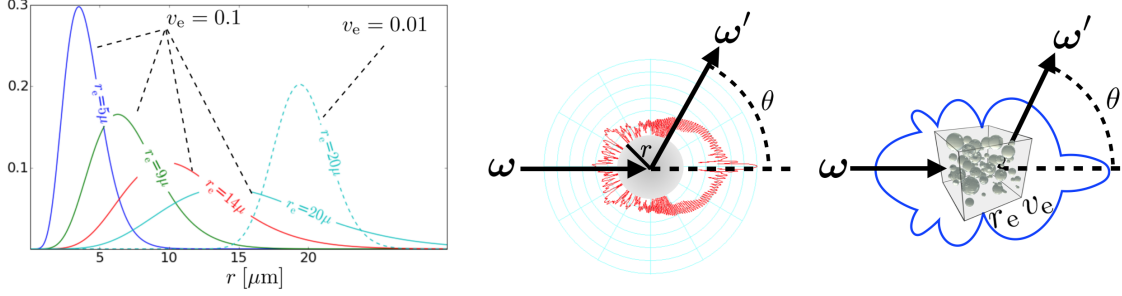


Figure 2: [Left] Normalized *Gamma*-distribution. The effective radius and variance dictate the centroid and width of the size-distribution. The limit of very low v_e approaches a mono-disperse distribution. [Center] Log-polar plot of the Mie phase-function p_{11} induced by a single water sphere of radius r . [Right] Log-polar plot of the effective phase-function $\langle s_s p_{11} \rangle_r / \sigma_s$ induced by a small volume that includes particles of different sizes.

and high-order scattered components. These foundations are used in subsequent sections, to formulate tomographic recovery.

2.1 Scatterer microphysical properties

In the lower atmosphere, cloud particles are droplets of liquid water that are very nearly spherical, having radius r . They are however polydisperse, with a droplet size distribution denoted $n(r)$. For most remote-sensing purposes, $n(r)$ is parameterized using an *effective radius* in μm and a dimensionless *variance* [39]:

$$r_e = \frac{\int_0^\infty r^3 n(r) dr}{\int_0^\infty r^2 n(r) dr}, \quad v_e = \frac{\int_0^\infty (r-r_e)^2 r^2 n(r) dr}{r_e^2 \int_0^\infty r^2 n(r) dr}. \quad (1)$$

A commonly used parametric size distribution, having empirical support [39] is the *Gamma*-distribution (Fig. 2):

$$n(r) = N c r^{(v_e^{-1}-3)} \exp[-r/(r_e v_e)], \quad (2)$$

where we require $v_e < 1/2$. Here $c = (r_e v_e)^{(2-v_e^{-1})} / \Gamma(v_e^{-1}-2)$ is a normalization constant and

$$N = \int_0^\infty n(r) dr \quad (3)$$

is the droplet number concentration. Let ρ_w be the density of liquid water. An important cloud characteristic is the water mass density or *Liquid Water Content* (LWC) per unit volume:

$$\text{LWC} = \frac{4}{3} \pi \rho_w \int_0^\infty r^3 n(r) dr. \quad (4)$$

It is expressed as $\text{LWC} = 4/3 \pi \rho_w r_e^3 (1 - v_e)(1 - 2v_e)$ for the Gamma distribution in (2).

2.2 Polarized light

A light wave is associated with orthogonal components of a random electric wave, $E_1(t)$ and $E_2(t)$, where t is time. The components' direction unit vectors are respectively $\hat{\mathbf{E}}_1$ and $\hat{\mathbf{E}}_2$. The wave propagates in direction $\boldsymbol{\omega} = \hat{\mathbf{E}}_1 \times \hat{\mathbf{E}}_2$. It is convenient to define the polarized light state in terms of the Stokes [39] vector $\mathbf{I} = (I, Q, U, V)^\top$. Each component of \mathbf{I} expresses temporal expectation:

$$\begin{aligned} I &= \langle E_1 E_1^* + E_2 E_2^* \rangle_t, & Q &= \langle E_1 E_1^* - E_2 E_2^* \rangle_t, \\ U &= \langle E_1 E_2^* + E_2 E_1^* \rangle_t, & V &= i \langle E_1 E_2^* - E_2 E_1^* \rangle_t, \end{aligned} \quad (5)$$

where $i = \sqrt{-1}$. Unpolarized intensity is I . The degrees of polarization (DOP) and linear polarization (DoLP) are respectively defined as the ratios $\sqrt{Q^2+U^2+V^2}/I$, $\sqrt{Q^2+U^2}/I$. The angle of linear polarization (AoLP) is $1/2 \tan^{-1}(U/Q)$.

2.3 Single scattering of polarized light

Light interaction with a single particle is described by the total extinction cross-section $s_t(r, \lambda)$, decomposed into scattering and absorption cross-sections, respectively:

$$s_t(r, \lambda) = s_s(r, \lambda) + s_a(r, \lambda). \quad (6)$$

In Mie scattering by spheres, introduced further on, we have

$$s_t(r, \lambda) = \pi r^2 Q_t(2\pi r/\lambda), \quad s_s(r, \lambda) = \pi r^2 Q_s(2\pi r/\lambda), \quad s_a(r, \lambda) = \pi r^2 Q_a(2\pi r/\lambda)$$

where Q_t , Q_s , Q_a are dimensionless efficiency factors, which depend on the normalized size parameter $2\pi r/\lambda$. In the limit $r \gg \lambda$, $Q_t \approx 2$. Furthermore, when $s_s(r, \lambda) \gg s_a(r, \lambda)$, then $Q_s \approx 2$ and $Q_a \approx 0$.

Define size-weighted average over some function $a(r)$ by³

$$\langle a \rangle_r = \frac{1}{N} \int_0^\infty a(r) n(r) dr. \quad (7)$$

Note that we use here an approximation, commonly used in multi-spectral remote sensing, of a single rendering with spectrally-averaged optical properties. The material optical properties can furthermore be approximated, in the absence of molecular absorption, by using a single wavelength for each spectral band. This is valid if wavelength dependencies within a spectral band are weak, a condition met when narrow bands are considered. Macroscopic optical cross-sections are then expressed as weighted averages⁴

$$\sigma_t(\lambda) = \langle s_t(r, \lambda) \rangle_r, \quad \sigma_s(\lambda) = \langle s_s(r, \lambda) \rangle_r, \quad \sigma_a(\lambda) = \langle s_a(r, \lambda) \rangle_r. \quad (8)$$

Throughout the text, dependency on λ is generally omitted for simplicity; however, it is used at specific points as needed.

Scattering, as a fraction of the overall interaction [40], is expressed by the dimensionless *single scattering albedo*

$$\varpi = \frac{\sigma_s}{\sigma_t}. \quad (9)$$

The extinction coefficient (or optical density) is denoted by β . Following Eqs. [3,4,8], $\beta = N\sigma_t$ is expressed in terms of the LWC as [41]

$$\beta = \frac{\text{LWC}}{\frac{4}{3}\pi\rho_w\langle r^3 \rangle_r} \sigma_t = \text{LWC} \cdot \tilde{\sigma}_t. \quad (10)$$

Here, $\tilde{\sigma}_t$ is the mass extinction coefficient (in units of m^2/g).

Let $\boldsymbol{\omega}$ and $\boldsymbol{\omega}'$ be the unitary incident and scattered ray direction vectors respectively in Fig. 2. Single-scattering geometry is defined by the local coordinate system of the incoming beam's electric fields. As stated above, the electric field of incoming light is decomposed into components along orthogonal directions. We set them as

$$\mathbf{E}_1 \propto \boldsymbol{\omega} \times \boldsymbol{\omega}', \quad \mathbf{E}_2 \propto \mathbf{E}_1 \times \boldsymbol{\omega}. \quad (11)$$

The scattering angle is $\theta = \cos^{-1}(\boldsymbol{\omega} \cdot \boldsymbol{\omega}')$. The angular redistribution of singly-scattering light from a sphere of is defined by the 4×4 dimensionless *Mueller matrix* $\mathbf{P}_s(\theta, r)$. The macroscopic *phase matrix* is the size-weighted average

$$\mathbf{P}(\theta) = \frac{\langle s_s(r) \mathbf{P}_s(\theta, r) \rangle_r}{\sigma_s}. \quad (12)$$

For spherical (or just randomly-oriented) particles, the phase-matrix $\mathbf{P}(\theta)$ takes the following symmetric form [39]

$$\mathbf{P}(\theta) = \begin{bmatrix} p_{11}(\theta) & p_{21}(\theta) & 0 & 0 \\ p_{21}(\theta) & p_{22}(\theta) & 0 & 0 \\ 0 & 0 & p_{33}(\theta) & -p_{43}(\theta) \\ 0 & 0 & p_{43}(\theta) & p_{44}(\theta) \end{bmatrix}, \quad (13)$$

where p_{11} is the (unpolarized) scattering phase-function. In single-scattering of unpolarized incident sunlight, the DoLP of scattered light amounts to the ratio $|p_{21}|/p_{11}$.

³ The size integral of (7) is in practice terminated at $r_{\max} = 70 \mu\text{m}$.

⁴ Aggregating scattered properties in (8) rather than electric fields holds for scatterer populations that are in each other's far field (i.e., are $\gg \lambda$ apart) [39].

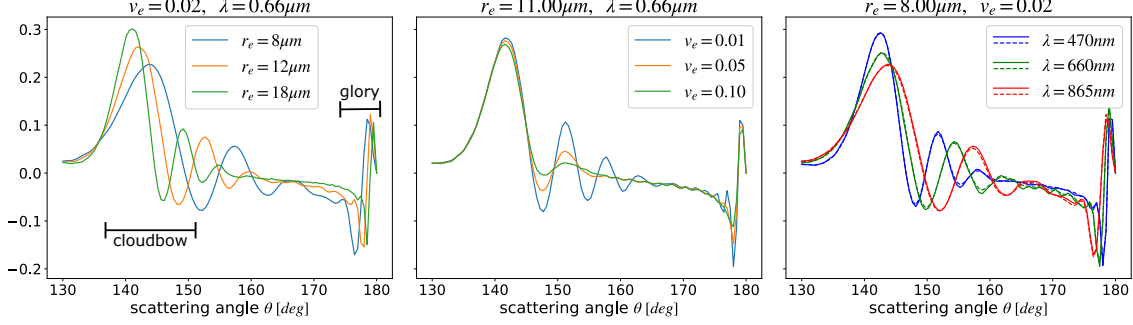


Figure 3: Normalized phase matrix element $-p_{12}^{\text{Mie}}/p_{11}^{\text{Mie}}$ around the cloud-bow and glory regions. For highly disperse droplet distributions (large v_e) the secondary lobes of the cloud-bow ($\theta \sim 140^\circ$) and glory ($\theta \sim 180^\circ$) diminish. The main cloud-bow peak is slightly sensitive to λ and v_e . The side-lobe angles are more sensitive to λ and r_e . The side-lobe amplitude is sensitive to v_e . This cloud-bow signal is helpful for retrievals of r_e . [Right plot] Solid lines indicate monochromatic light. Dashed lines indicate spectral averaging over a 100 nm bandwidth, which is more than double any of the spectral bands considered further on.

2.3.1 Rayleigh scattering

The Rayleigh model describes light scattering by particles much smaller than the wavelength. The Rayleigh phase matrix takes the following form [42]

$$\mathbf{P}_{\text{Rayl}}(\theta) = \begin{bmatrix} \frac{3}{4}(1 + \cos^2 \theta) & -\frac{3}{4}\sin^2 \theta & 0 & 0 \\ -\frac{3}{4}\sin^2 \theta & \frac{3}{4}(1 + \cos^2 \theta) & 0 & 0 \\ 0 & 0 & \frac{3}{2}\cos \theta & 0 \\ 0 & 0 & 0 & \frac{3}{2}\cos \theta \end{bmatrix}. \quad (14)$$

The single-scattering DoLP due to air molecules is then

$$\text{DoLP}_{\text{Rayl}}(\theta) = \frac{\sin^2 \theta}{1 + \cos^2 \theta}. \quad (15)$$

According to (15) a maximum DoLP is attained at single-scattering angle $\theta = 90^\circ$.

2.3.2 Mie scattering

Mie theory describes how light interacts with a spherical particle of size comparable to λ [43]. Denote $\mu = \cos \theta$. Mie scattering is defined in terms of complex-valued amplitude scattering functions⁵ $S_1(\mu), S_2(\mu)$, which correspond to scattering of the E_1, E_2 electric field components. Scattering of the Stokes vector \mathbf{I} is described by the phase matrix $\mathbf{P}_{\text{Mie}}(\mu)$, which is fully defined by six matrix components:

$$\begin{aligned} p_{11}^{\text{Mie}} &= \frac{\varrho}{2}(S_1 S_1^* + S_2 S_2^*), & p_{12}^{\text{Mie}} &= \frac{\varrho}{2}(S_1 S_1^* - S_2 S_2^*), \\ p_{22}^{\text{Mie}} &= \frac{\varrho}{2}(S_1 S_1^* + S_2 S_2^*), & p_{33}^{\text{Mie}} &= \frac{\varrho}{2}(S_1 S_2^* + S_2 S_1^*), \\ p_{43}^{\text{Mie}} &= \frac{\varrho}{2}(S_1 S_2^* - S_2 S_1^*), & p_{44}^{\text{Mie}} &= \frac{\varrho}{2}(S_1 S_2^* + S_2 S_1^*). \end{aligned}$$

Here, ϱ is a normalization constant, set to satisfy $\frac{1}{2} \int_{-1}^1 p_{11}^{\text{Mie}}(\mu) d\mu = 1$.

Mie scattering due to water droplets is peaked at specific angles. For a single droplet or monodisperse material, \mathbf{P}^{Mie} has sharp scattering lobes at angles that depend on the droplet's r/λ ratio. A macroscopic voxel contains droplets in a range of radii r , smoothing the scattering lobes. The smoothing effect depends on v_e (Fig. 3) and, to a far lesser extent, the spectral bandwidth (Fig. 3). Two angular domains that stand out for remote-sensing purposes are the cloud-bow ($\theta \in [135^\circ, 155^\circ]$) and glory ($\theta \in [175^\circ, 180^\circ]$). Both domains have peaks that are sensitive to the droplet microphysical parameters, and are significantly polarized (i.e., peaks are visible in the p_{12}^{Mie} component). The latter fact renders these peaks distinguishable in the presence of a multiply-scattered signal component.

⁵ For a full mathematical description, see [43].

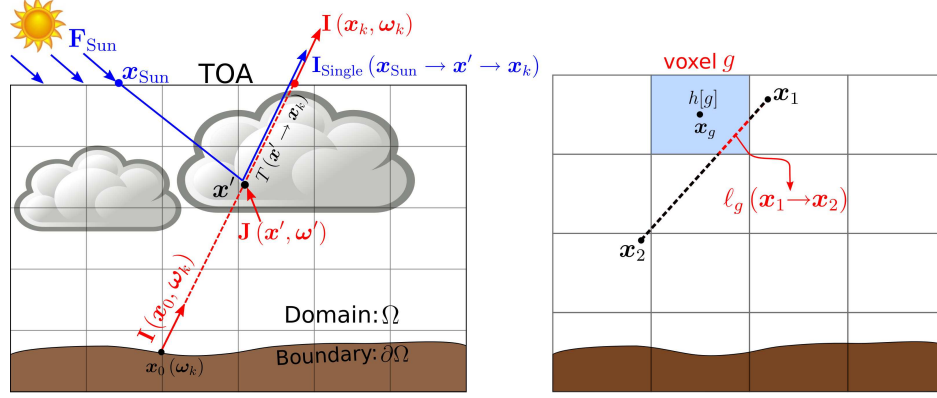


Figure 4: [Left] Light scatters in the medium, generally multiple times, creating a partially polarized (vector) scatter field \mathbf{J} ((18)). Integration yields the partially polarized (vector) light field \mathbf{I} ((17)). Here $I(x_k, \omega_k)$ is a pixel measurement at the TOA and $\mathbf{I}_{\text{Single}}$ is the single-scattered contribution from x' [Right] Ray tracing of a line-integral over a discretized voxel field $h[g]$ (zero-order interpolation).

2.4 Multiple scattering of polarized light

The *Radiative Transfer Equation* (RTE) [42] describes multiple scattering interactions of monochromatic partially polarized light within a medium. Transmittance between two points x_1, x_2 is

$$T(x_1 \rightarrow x_2) = \exp \left[- \int_{x_1}^{x_2} \beta(x) dx \right]. \quad (16)$$

An atmospheric domain Ω has boundary $\partial\Omega$. The intersection of $\partial\Omega$ with a ray originating at point x in direction $-\omega$ (Fig. 4) is denoted $x_0(x, \omega)$. Denote the Stokes vector field as $\mathbf{I}(x, \omega)$. Then $\mathbf{I}(x_0, \omega)$ is the Stokes vector of radiation which propagates in direction ω at boundary point $x_0(x, \omega)$. The non-emissive forward RT model [42] couples $\mathbf{I}(x, \omega)$ to a vector *source field* $\mathbf{J}(x, \omega)$ (Fig. 4) by

$$\mathbf{I}(x, \omega) = \mathbf{I}(x_0, \omega) T(x_0 \rightarrow x) + \int_{x_0}^x \mathbf{J}(x', \omega) \beta(x') T(x' \rightarrow x) dx', \quad (17)$$

$$\mathbf{J}(x, \omega) = \frac{\varpi(x)}{4\pi} \int_{4\pi} \mathbf{P}(x, \omega \cdot \omega') \mathbf{I}(x, \omega') d\omega'. \quad (18)$$

Equations [17-18] are solved numerically, either directly with an explicit solver [35] or indirectly using a Monte-Carlo path tracer [44]. We use vSHDOM [35] to simulate scattered Stokes components of a realistic atmosphere, having both Mie and Rayleigh scattering due to water droplets and air molecules.

Multiple scattering interactions are defined using two coordinate systems. Local *scatterer coordinates* are set by $(\hat{\mathbf{E}}_1, \hat{\mathbf{E}}_2)$. Stokes measurements in satellites, however, are defined in *Meridional* coordinates. Let $\hat{\mathbf{z}}$ denote the zenith direction vector at every point on Earth. In meridian coordinates, the electric field components are defined by direction vectors

$$\hat{\mathbf{m}}_1 = \frac{\hat{\mathbf{z}} \times \omega}{\|\hat{\mathbf{z}} \times \omega\|}, \quad \hat{\mathbf{m}}_2 = \omega \times \hat{\mathbf{m}}_1. \quad (19)$$

Each pixel-scale Stokes measurement is described by a coordinate system defined by $\hat{\mathbf{m}}_1$ and $\hat{\mathbf{m}}_2$. The transformation between the two coordinate systems amounts to a multiplication of \mathbf{I} by a Mueller rotation matrix.

Sampling $\mathbf{I}(x, \omega)$ at the location of each camera and direction of each camera pixel yields the measured Stokes vector. A measurement k is done at the camera position x_k , LOS direction ω_k , and wavelength λ_k (Fig. 4). Thus, Eqs. [17-18] yield the pixel measurement model

$$\mathbf{I}[k] = \mathbf{I}(x_0, \omega_k) T(x_0 \rightarrow x_k) + \int_{x_0}^{x_k} \mathbf{J}(x', \omega_k) \beta(x') T(x' \rightarrow x_k) dx'. \quad (20)$$

2.5 Single-scattering separation

It is often convenient to separate the single-scattering contribution from the rest of the radiance field [45]. The solar irradiance at the top of the atmosphere (TOA) is F_{Sun} . It is unpolarized, thus corresponds to a Stokes vector

$\mathbf{F}_{\text{Sun}} = (F_{\text{Sun}}, 0, 0, 0)^\top$. The Sun is modeled as an ideal directional source with direction $\boldsymbol{\omega}_{\text{Sun}}$. A solar ray heading to point \mathbf{x} intersects the TOA at point \mathbf{x}_{Sun} . The solar transmittance is given by $T(\mathbf{x}_{\text{Sun}} \rightarrow \mathbf{x})$. Let δ denote *Dirac's delta*. Thus, \mathbf{I} can be written as a sum of the *diffuse* component \mathbf{I}_d , and direct solar component:

$$\mathbf{I}(\mathbf{x}, \boldsymbol{\omega}) = \mathbf{I}_d(\mathbf{x}, \boldsymbol{\omega}) + \delta(\boldsymbol{\omega} - \boldsymbol{\omega}_{\text{Sun}}) \mathbf{F}_{\text{Sun}} T(\mathbf{x}_{\text{Sun}} \rightarrow \mathbf{x}). \quad (21)$$

Inserting [21] into [18] yields

$$\mathbf{J}(\mathbf{x}, \boldsymbol{\omega}) = \mathbf{J}_d(\mathbf{x}, \boldsymbol{\omega}) + \frac{\varpi(\mathbf{x})}{4\pi} \mathbf{P}(\mathbf{x}, \boldsymbol{\omega} \cdot \boldsymbol{\omega}_{\text{Sun}}) \mathbf{F}_{\text{Sun}} T(\mathbf{x}_{\text{Sun}} \rightarrow \mathbf{x}), \quad (22)$$

where

$$\mathbf{J}_d(\mathbf{x}, \boldsymbol{\omega}) = \frac{\varpi(\mathbf{x})}{4\pi} \int_{4\pi} \mathbf{P}(\mathbf{x}, \boldsymbol{\omega} \cdot \boldsymbol{\omega}') \mathbf{I}_d(\mathbf{x}, \boldsymbol{\omega}') d\boldsymbol{\omega}'. \quad (23)$$

Consider Fig. 4. Denote a *broken-ray* path of direct sunlight which undergoes single scattering at \mathbf{x}' , then reaches the camera:

$$\mathbf{x}_{\text{Sun}} \rightarrow \mathbf{x}' \rightarrow \mathbf{x}_k. \quad (24)$$

It projects in direction $\boldsymbol{\omega}_k$ to pixel at \mathbf{x}_k , thus contributing to the measurement $\mathbf{I}(\mathbf{x}_k, \boldsymbol{\omega}_k)$. Using Eqs. [17,22], the single-scattered contribution from \mathbf{x}' is

$$\mathbf{I}_{\text{Single}}(\mathbf{x}_{\text{Sun}} \rightarrow \mathbf{x}' \rightarrow \mathbf{x}_k) = \frac{\varpi(\mathbf{x}')}{4\pi} \beta(\mathbf{x}') \mathbf{P}(\mathbf{x}', \boldsymbol{\omega}_k \cdot \boldsymbol{\omega}_{\text{Sun}}) \mathbf{F}_{\text{Sun}} T(\mathbf{x}_{\text{Sun}} \rightarrow \mathbf{x}') T(\mathbf{x}' \rightarrow \mathbf{x}_k). \quad (25)$$

Thus, the entire single-scattered signal accumulates contributions along the LOS

$$\mathbf{I}_{\text{Single}}(\mathbf{x}_k) = \int_{\mathbf{x}_0}^{\mathbf{x}_k} \mathbf{I}_{\text{Single}}(\mathbf{x}_{\text{Sun}} \rightarrow \mathbf{x}' \rightarrow \mathbf{x}_k) d\mathbf{x}'. \quad (26)$$

2.6 Ray tracing

Ray tracing computes a function over a straight line through a 3D domain. A common operation is path-integration (e.g. Eqs. [16,17]). Let $h(\mathbf{x})$ be a continuous field. Define a grid of discrete points \mathbf{x}_g , where $g = 1, 2, \dots, N_{\text{grid}}$. Denote $h[g] = h(\mathbf{x}_g)$. A path-integral over $h(\mathbf{x})$ is numerically computed using an interpolation kernel K

$$\int_{\mathbf{x}_1}^{\mathbf{x}_2} h(\mathbf{x}) d\mathbf{x} = \sum_{g=1}^{N_{\text{grid}}} h[g] \int_{\mathbf{x}_1}^{\mathbf{x}_2} K(\mathbf{x} - \mathbf{x}_g) d\mathbf{x}. \quad (27)$$

For zero-order interpolation (i.e., voxel grid), (27) degenerates to

$$\int_{\mathbf{x}_1}^{\mathbf{x}_2} h(\mathbf{x}) d\mathbf{x} = \sum_{g=1}^{N_{\text{grid}}} h[g] \ell_g(\mathbf{x}_1 \rightarrow \mathbf{x}_2), \quad (28)$$

where $\ell_g(\mathbf{x}_1 \rightarrow \mathbf{x}_2)$ is the intersection of the path with voxel g (Fig. 4). For voxel indices g that do not intersect the path $\mathbf{x}_1 \rightarrow \mathbf{x}_2$, the value of $\ell_g(\mathbf{x}_1 \rightarrow \mathbf{x}_2)$ is 0.

sectionCloud Tomography So far, we described the forward (image-formation) model, i.e., how images are formed, given cloud properties. In this work, we formulate a novel inverse tomographic problem of recovering the unknown cloud microphysical properties, volumetrically. In voxel g , the vector of unknown parameters is $(\text{LWC}[g], r_e[g], v_e[g])$. The unknown microphysical parameters are concatenated to a vector of length $3N_{\text{grid}}$

$$\boldsymbol{\Theta} = (\dots, \text{LWC}[g], r_e[g], v_e[g], \dots)^\top, \quad 1 \leq g \leq N_{\text{grid}}. \quad (29)$$

Neglecting circular polarization, each pixel measures a Stokes vector, $\mathbf{y}_I = (y_I, y_Q, y_U)$ at N_λ wavelengths. Let N_{views} and N_{pix} denote the number of view points and camera pixels. The total number of Stokes measurements is thus $N_{\text{meas}} = N_\lambda N_{\text{views}} N_{\text{pix}}$. The measurement vector of length $3N_{\text{meas}}$ is expressed as

$$\mathbf{y} = (\mathbf{y}_I[1], \dots, \mathbf{y}_I[N_{\text{meas}}])^\top. \quad (30)$$

In this section, we formulate the use of measurements \mathbf{y} (multi-view, multi-pixel, multi-spectral, polarimetric measurements) for tomographic retrieval of $\boldsymbol{\Theta}$ (3D volumetric cloud density and microphysics). It is worth mentioning at this point that Stokes components are not measured directly. Rather, they are computationally retrieved from measurements of different polarization states (see *Appendix* for the AirMSPI measurement model).

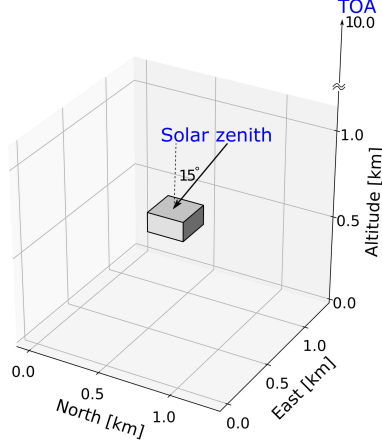


Figure 5: A homogeneous cubic cloud illuminated with solar radiation at a zenith angle of 15° off-nadir. The solar azimuth angles are $\phi_0 = [0.0^\circ, 67.5^\circ]$. The outgoing Stokes vector \mathbf{I} is simulated at AirMSPI resolution and wavelengths, with AirMSPI measuring along a North-bound track.

2.7 Polarimetric information

To make an initial assessment of the sensitivity of polarimetric measurements, we simulate a simple homogeneous cubic cloud (Fig. 5), parameterized by two microphysical parameters: (LWC, r_e) . Back-scattered Stokes measurements are taken at the TOA for angles and wavelengths sampled by the Airborne Multi-angle Spectro-Polarimetric Imager (AirMSPI) [14]. Define $I[k], U[k], Q[k]$ as simulated Stokes components at measurement index k . Define a cost function for each of the Stokes components

$$\mathcal{D}_I(LWC, r_e) = \sum_{k=1}^{N_{\text{meas}}} (I[k] - y_I[k])^2, \quad (31)$$

$$\mathcal{D}_Q(LWC, r_e) = \sum_{k=1}^{N_{\text{meas}}} (Q[k] - y_Q[k])^2, \quad (32)$$

$$\mathcal{D}_U(LWC, r_e) = \sum_{k=1}^{N_{\text{meas}}} (U[k] - y_U[k])^2, \quad (33)$$

where we hold v_e constant. Equations [31-33] are 2D manifolds. Figure 6 plots the cost manifolds for different solar azimuth angles, ϕ_0 . While there is an ambiguity between LWC and r_e when relying on \mathcal{D}_I , there are better defined minima for \mathcal{D}_Q and \mathcal{D}_U . This indicates that polarization measurements carry valuable information.

2.8 Inverse problem formulation

Denote \mathbf{I}_Θ as the image formation model. Tomography can be formulated as minimization of a data-fit function. We preform

$$\hat{\Theta} = \arg \min_{\Theta} \mathcal{D}(\mathbf{I}_\Theta, \mathbf{y}) = \arg \min_{\Theta} (\mathbf{I}_\Theta - \mathbf{y})^\top \Sigma^{-1} (\mathbf{I}_\Theta - \mathbf{y}), \quad (34)$$

Here Σ is related to the co-variance of the measurement noise. For brevity, we omit the subscript Θ but remember that

$$\mathbf{I} \equiv \mathbf{I}_\Theta, \quad \mathbf{J} \equiv \mathbf{J}_\Theta, \quad \beta \equiv \beta_\Theta, \quad \varpi \equiv \varpi_\Theta, \quad \mathbf{P} \equiv \mathbf{P}_\Theta, \quad T \equiv T_\Theta. \quad (35)$$

Assuming noise in different pixels, wavelengths and angles is uncorrelated, (34) degenerates to

$$\hat{\Theta} = \arg \min_{\Theta} \sum_{k=1}^{N_{\text{meas}}} (\mathbf{I}[k] - \mathbf{y}_I[k])^\top \mathbf{R}^{-1} (\mathbf{I}[k] - \mathbf{y}_I[k]). \quad (36)$$

The matrix \mathbf{R} depends on the particular sensor technology. Description of \mathbf{R} , tailored to the AirMSPI sensor, is detailed in the *Appendix*.

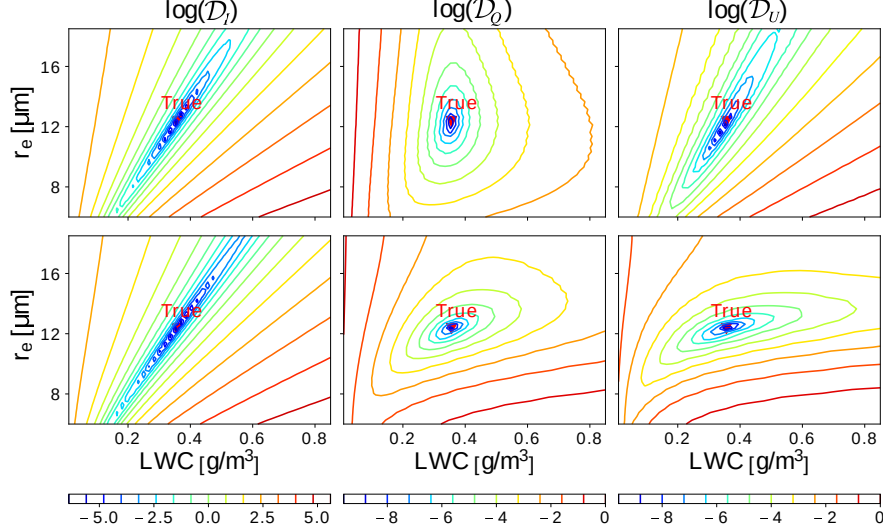


Figure 6: Logarithm of the 2D cost manifolds for a 2-parameter homogeneous cubic cloud (Fig. 5). Each column of plots corresponds to the cost of the different Stokes components in Eqs. [31-33]. Each row of plots corresponds to a different Solar azimuth angle ϕ_0 .

We solve (36) by a gradient-based approach. The gradient with respect to the unknown parameters Θ is

$$\nabla_{\Theta} \mathcal{D}(\mathbf{I}_{\Theta}, \mathbf{y}) = 2 \sum_{k=1}^{N_{\text{meas}}} (\mathbf{I}[k] - \mathbf{y}_{\mathbf{I}}[k])^{\top} \mathbf{R}^{-1} \nabla_{\Theta} \mathbf{I}[k]. \quad (37)$$

The term $\nabla_{\Theta} \mathbf{I}[k]$ is the *Jacobian* of the sensing model. Equation [37] is used to formulate an update rule for an iterative optimization algorithm

$$\Theta_{b+1} = \Theta_b - \chi_b \nabla_{\Theta} \mathcal{D}(\mathbf{I}_{\Theta}, \mathbf{y}), \quad (38)$$

where b denotes the iteration index and χ_b is a scalar. We use L-BFGS [46] for numerical optimization that, in particular, determines adaptively the value of χ_b . One approach to computing the gradient $\nabla_{\Theta} \mathcal{D}$ is the *Adjoint RTE* [47, 48]. Due to the recursive nature of the RTE, computing the gradient through the exact Jacobian $\nabla_{\Theta} \mathbf{I}[k]$ is computationally expensive. In the following sections, we derive a method to make the computation of the gradient tractable and efficient. We do that by approximating the Jacobian $\nabla_{\Theta} \mathbf{I}$ in a tractable way, using a two-step iterative algorithm [36, 38].

2.9 Iterative solution approach

We formulate an iterative algorithm which alternates between two steps (See the diagram in Fig. 7). Starting with an initial guess, Θ_0 , Step 1 uses vSHDOM to compute the forward (recursive) RT equations. This renders synthetic images according to the multi-view geometry, spectral bands and spatial samples of the cameras. Keeping \mathbf{I}_d fixed, Step 2 efficiently computes an approximate gradient with respect to Θ . The approximate gradient is fed into an L-BFGS step to update the current estimate Θ_b .

Step 1: RTE Forward Model

The first step in the estimation approach is running the forward model in Eqs. [17-18] using a numerical RTE solver. This requires transforming microphysical to optical properties at every voxel (g) and spectral band (λ):

$$\text{LWC}[g], r_e[g], v_e[g] \longrightarrow \beta_{\lambda}[g], \varpi_{\lambda}[g], \mathbf{P}_{\lambda}[g]. \quad (39)$$

Implementing (39) using Eqs. [8-12] during each optimization iteration can be time-consuming. Therefore, define grids $r_e \in [r_e^{\min}, \dots, r_e^{\max}]$ and $v_e \in [v_e^{\min}, \dots, v_e^{\max}]$, for which lookup tables $\tilde{\sigma}_{\lambda}(r_e, v_e)$, $\varpi_{\lambda}(r_e, v_e)$, $\mathbf{P}_{\lambda}(r_e, v_e)$ are pre-computed. With these pre-computed tables and $\{\text{LWC}[g], r_e[g], v_e[g]\}$, vSHDOM [35] renders the Stokes vector at each 3D voxel and direction. This is the forward modeling procedure. The result is the set of fields $\mathbf{I}(\mathbf{x}, \omega)$, $\mathbf{I}_d(\mathbf{x}, \omega)$, $\mathbf{J}(\mathbf{x}, \omega)$, $\mathbf{I}_{\text{Single}}(\mathbf{x}_{\text{Sun}} \rightarrow \mathbf{x}' \rightarrow \mathbf{x}_k)$.

Step 2: Approximate Jacobian Computation

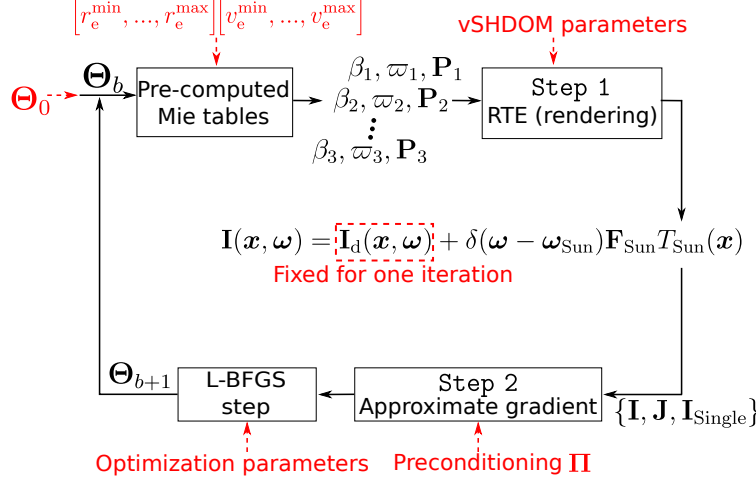


Figure 7: A block diagram of the iterative algorithm. Red marks hyper-parameter. Numerical parameters of vSHDOM and L-BFGS are summarized in the .

The forward vRTE model in (20) depends on optical properties $(\beta, \varpi, \mathbf{P})$, which themselves depend on the sought microphysics. The Jacobian at voxel g is expressed by applying the chain-rule to (20). For example, the derivative with respect to the effective radius is

$$\frac{\partial \mathbf{I}[k]}{\partial r_e[g]} = \frac{\partial \mathbf{I}[k]}{\partial \beta[g]} \frac{\partial \beta[g]}{\partial r_e[g]} + \frac{\partial \mathbf{I}[k]}{\partial \varpi[g]} \frac{\partial \varpi[g]}{\partial r_e[g]} + \frac{\partial \mathbf{I}[k]}{\partial \mathbf{P}[g]} \frac{\partial \mathbf{P}[g]}{\partial r_e[g]}. \quad (40)$$

Analogously, replacing r_e in (40) with LWC or v_e yields the respective microphysical derivatives. We proceed by expressing the derivatives $\partial\{\beta, \varpi, \mathbf{P}\}/\partial\{\text{LWC}, r_e, v_e\}$. Afterwards, we expand and combine the derivatives $\partial \mathbf{I}/\partial\{\beta, \varpi, \mathbf{P}\}$ to express (40).

For each voxel, the derivatives of $(\beta, \varpi, \mathbf{P})$ with respect to the microphysics are calculated using pre-computed tables

$$\frac{\partial \beta}{\partial \text{LWC}} = \tilde{\sigma}(r_e, v_e), \quad \frac{\partial \beta}{\partial r_e} = \frac{\tilde{\sigma}(r_e + \varepsilon_{r_e}, v_e) - \tilde{\sigma}(r_e, v_e)}{\varepsilon_{r_e}}, \quad (41)$$

$$\frac{\partial \varpi}{\partial \text{LWC}} = 0, \quad \frac{\partial \varpi}{\partial r_e} = \frac{\varpi(r_e + \varepsilon_{r_e}, v_e) - \varpi(r_e, v_e)}{\varepsilon_{r_e}}, \quad (42)$$

$$\frac{\partial \mathbf{P}}{\partial \text{LWC}} = 0, \quad \frac{\partial \mathbf{P}}{\partial r_e} = \frac{\mathbf{P}(r_e + \varepsilon_{r_e}, v_e) - \mathbf{P}(r_e, v_e)}{\varepsilon_{r_e}}, \quad (43)$$

where v_e derivatives are computed analogously to the r_e derivatives. Using the shorthand notation $\partial_g \equiv \left\{ \frac{\partial}{\partial \text{LWC}[g]}, \frac{\partial}{\partial r_e[g]}, \frac{\partial}{\partial v_e[g]} \right\}$, the overall Jacobian is given by a sum of terms

$$\partial_g \mathbf{I}[k] = A_1 + A_2 + A_3 + A_4 + A_5 + A_6. \quad (44)$$

The full expression for each term in Eq. [44] is given in the *Appendix*. For example,

$$A_1 = -\ell_g(\mathbf{x}_0 \rightarrow \mathbf{x}_k) \mathbf{I}(\mathbf{x}_0, \boldsymbol{\omega}_k) T(\mathbf{x}_0 \rightarrow \mathbf{x}_k) [\partial_g \beta]. \quad (45)$$

Let us focus on the term

$$A_4 = \int_{\mathbf{x}_0}^{\mathbf{x}_k} \left\{ \frac{\varpi(\mathbf{x}')}{4\pi} \int_{4\pi} \mathbf{P}(\mathbf{x}', \boldsymbol{\omega}_k \cdot \boldsymbol{\omega}') [\partial_g \mathbf{I}(\mathbf{x}', \boldsymbol{\omega}')] d\boldsymbol{\omega}' \right\} \beta(\mathbf{x}') T(\mathbf{x}' \rightarrow \mathbf{x}_k) d\mathbf{x}'. \quad (46)$$

This Jacobian term stands out, because it is only term which requires computing the derivative of \mathbf{I} . This derivative is computationally expensive because \mathbf{I} is computed recursively through the RTE [Eqs. 17-18]. In principle, a change in the microphysics of one voxel can recursively affect the radiance at every other voxel. We decompose $\partial_g \mathbf{I}$ using the diffuse-direct decomposition of (21)

$$\partial_g \mathbf{I}(\mathbf{x}', \boldsymbol{\omega}') = \partial_g \mathbf{I}_d(\mathbf{x}', \boldsymbol{\omega}') + \delta(\boldsymbol{\omega}' - \boldsymbol{\omega}_{\text{Sun}}) \mathbf{F}_{\text{Sun}} [\partial_g T(\mathbf{x}_{\text{Sun}} \rightarrow \mathbf{x}')]. \quad (47)$$

At the core our approach for computational efficiency is the assumption that the diffuse light \mathbf{I}_d is less sensitive to slight changes in the microphysical properties of any single voxel g . Rather, \mathbf{I}_d is impacted mainly by bulk changes to

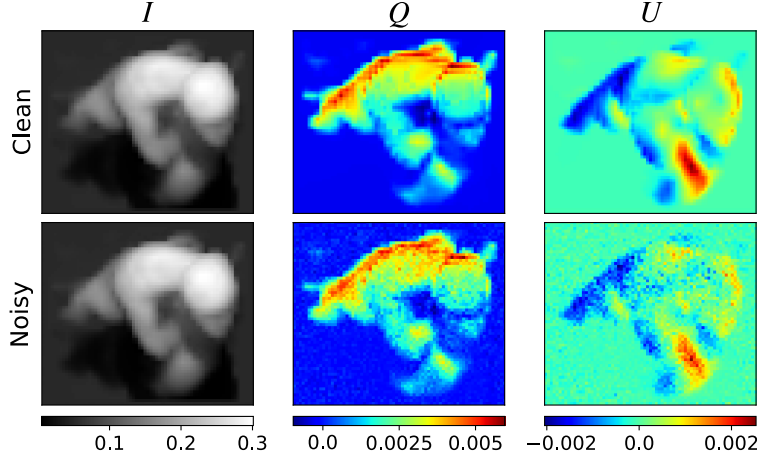


Figure 8: Scene A synthesized Stokes image using vSHDOM, before and after the application of a realistic AirMSPI noise model. We show here the *Bidirectional Reflectance Factor* (BRF) of the nadir view at $\lambda=0.67\mu\text{m}$.

the over-all volume. Thus, we approximate (46) by keeping \mathbf{I}_d independent of Θ for a single iteration of the gradient computation, i.e.,

$$\partial_g \mathbf{I}_d \approx 0. \quad (48)$$

This bypasses the complexity of recursively computing $\partial_g \mathbf{I}_d$.

It is important to note that at every iteration, the Jacobian $\nabla_{\Theta} \mathbf{I}[k]$ still is impacted by \mathbf{I}_d . This is because \mathbf{I}_d affects \mathbf{I} through Eq. [21], and \mathbf{I} appears in the terms A_1, \dots, A_6 . As the estimated medium properties evolve through iterations, so does \mathbf{I}_d (in Step 1, above). We just assume during Step 2 that $\partial_g \mathbf{I}_d$ is negligible compared to other terms in Eq. [44].

Contrary to \mathbf{I}_d , the single-scattered component is highly sensitive to changes in the micro-physical properties of a single voxel. We therefore include an exact treatment of single-scattering in the gradient computation (in the *Appendix*). This is the essence of our numerical optimization approach. It enables tackling multiple-scattering tomography, in practice. Simulation results presented in the following section rely on additional numerical considerations (e.g., initialization, preconditioning, convergence criteria), which are all described in the accompanying *Appendix*.

3 Simulations

As mentioned, real data of simultaneous spaceborne multi-angular polarimetric images of clouds does not yet exist, but a mission to supply this data is in the works. Therefore, we use careful simulations to test the approach. We simulate an atmosphere with molecular Rayleigh scattering and liquid water clouds. Rayleigh scattering is taken from the AFGL database [49] for a summer mid-latitude atmosphere. Mie tables are pre-computed for $r_e \in [4, 25] \mu\text{m}$ and $v_e = 0.1$ with $N_{r_e} = 100$. The surface is Lambertian with a water-like albedo of 0.05. For realistic complexity, a Large Eddy Simulation (LES) model [50] was used to generate a cloud field. Each voxel is of size $20 \times 20 \times 40 \text{ m}^3$. The LES outputs [50] are clouds with 3D variable LWC and 1D (vertically) variable r_e . A typical value [51] of $v_e = 0.1$ was chosen. Consequently, the present recovery demonstrations recover LWC and r_e on their respective native LES grid. On the other hand, $v_e = 0.1$ is excluded from the unknowns.

From the generated cloud field, two isolated cloudy regions are taken for reconstruction:

1. Scene A: An atmospheric domain of dimensions $0.64 \times 0.72 \times 20 \text{ km}^3$ with an isolated cloud (see synthetic AirMSPI nadir view in Fig. 8).
2. Scene B: An atmospheric domain of dimensions $2.42 \times 2.1 \times 8 \text{ km}^3$ with several clouds of varying optical thickness (see synthetic AirMSPI nadir view in Fig. 9).

Synthetic measurements rendered with the spatial resolution and angular sampling of AirMSPI [14], namely, 10 m pixels and 9 viewing angles: $\pm 70.5^\circ$, $\pm 60^\circ$, $\pm 45.6^\circ$, $\pm 26.1^\circ$, and 0° from zenith, where \pm indicates fore- and aft-views along the northbound flight path. Solar zenith angle is 15° from nadir in the measurement plane, i.e., 0° solar azimuth. We simulate measurements at AirMSPI's three polarized spectral bands: $\lambda = [0.47, 0.66, 0.865] \mu\text{m}$. The bandwidths are narrow enough ($\approx 46 \text{ nm}$) to render images using a single representative wavelength per band.

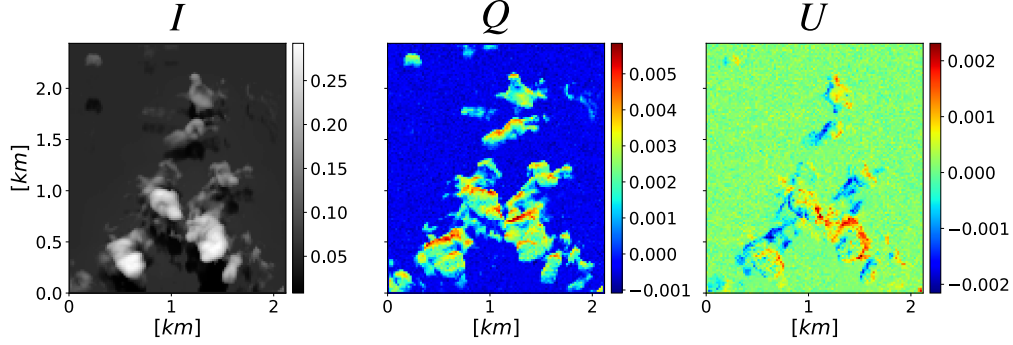


Figure 9: Scene B synthesized Stokes using vSHDOM. We show here the BRF of the nadir view at $\lambda=0.67\mu\text{m}$.

Single scattering albedos for these wavelengths are all within 10^{-4} of unity. In other words, and in sharp contrast with the operational Nakajima–King [9] bi-spectral non-tomographic retrieval, absorption by droplets plays no role in this demonstration of tomography of cloud microphysics. The measurements are synthesized with realistic noise, according to the AirMSPI data acquisition model (see *Appendix*).

Qualitative volumetric results of the recovered LWC for Scene A are shown in Fig. 10. Scatter plot of the recovered LWC and the recovery results of r_e for Scene A are given in Fig. 12. Analogous plots for Scene B recovery results are given in the *Appendix*.

For quantitative assessment of the recovery, we use local mean error ϵ , and global bias measures [52] ϑ :

$$\epsilon_{\text{LWC}} = \frac{\|\hat{\text{LWC}} - \text{LWC}\|_1}{\|\text{LWC}\|_1}, \quad \vartheta_{\text{LWC}} = \frac{\|\hat{\text{LWC}}\|_1 - \|\text{LWC}\|_1}{\|\text{LWC}\|_1}, \quad \epsilon_{r_e} = \frac{\|\hat{r}_e - r_e\|_1}{\|r_e\|_1}. \quad (49)$$

The quantitative error measures upon convergence for the two scenes are:

Scene A: $\epsilon_{r_e} \approx 11\%$, $\epsilon_{\text{LWC}} \approx 30\%$, $\vartheta_{\text{LWC}} \approx -4\%$,

Scene B: $\epsilon_{r_e} \approx 13\%$, $\epsilon_{\text{LWC}} \approx 29\%$, $\vartheta_{\text{LWC}} \approx -5\%$.

Using a 2.50 GHz CPU, the recovery run-time of cloud properties in Scenes A,B was ~ 13 hours and ~ 10 days, respectively.

Multi-angular tomographic retrieval enables vertical resolution of the droplet effective radius. By contrast, a homogeneous droplet radius is typically retrieved by mono-angular observations fitted to a plane-parallel homogeneous cloud model. The retrieval errors of droplet radii in the demonstrations above are significantly smaller than retrieval errors of a homogeneous droplet radius. The latter can easily exceed 50% in similar conditions to our study i.e, shallow cumuli and illumination conditions (see e.g. [53]).

4 Summary & Outlook

We derive tomography of cloud microphysics based on multi-view/multi-spectral polarimetric measurements of scattered sunlight. This novel type of tomography uses, for the first time, 3D polarized RT as the image formation model. We define a model-fitting error function and compute approximate gradients of this function to make the recovery tractable. Demonstration are done on synthetic 3D clouds, based on a Large Eddy Simulation with the effective radius assumed to vary only vertically.

Future work will address the extent to which polarimetric measurements penetrate the cloud and the relation between r_e in the *outer shell* and r_e in the *cloud core*, as defined by Forster et al. [54]. Furthermore, we will relax the fixed v_e assumption that was used in the demonstrations, and thus assess full microphysical retrieval capabilities of polarization measurements. A thorough discussion on these assumptions and their applicability to real-world clouds is given in the *Appendix*. Moreover, future plans include experimental demonstration and use, while the CloudCT formation orbits.

Lastly, we note that our atmospheric tomography approach herein can be adapted to aerosols, including dense plumes of wild fire smoke, volcanic ash, and dust. Research is ongoing [54] about such adaptation for satellite data as can be obtained from the multi-view imaging from MISR on Terra and a SWIR view from the collocated MODIS, as well as in the planned CloudCT [8].

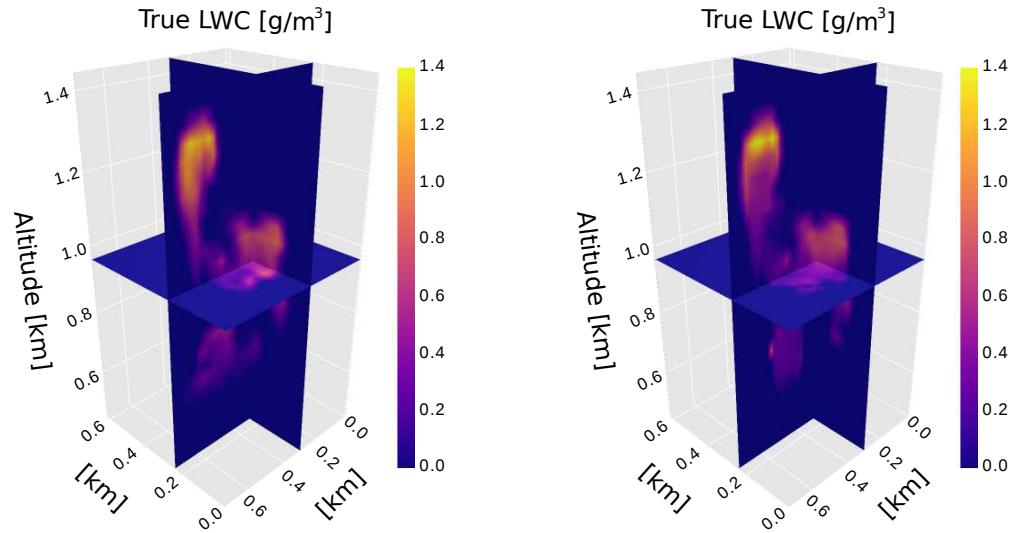


Figure 10: Scene A recovery results. [Left] Slices of the true cloud generated by LES. [Right] Slices of the cloud estimated tomographically using AirMSPI polarized bands.

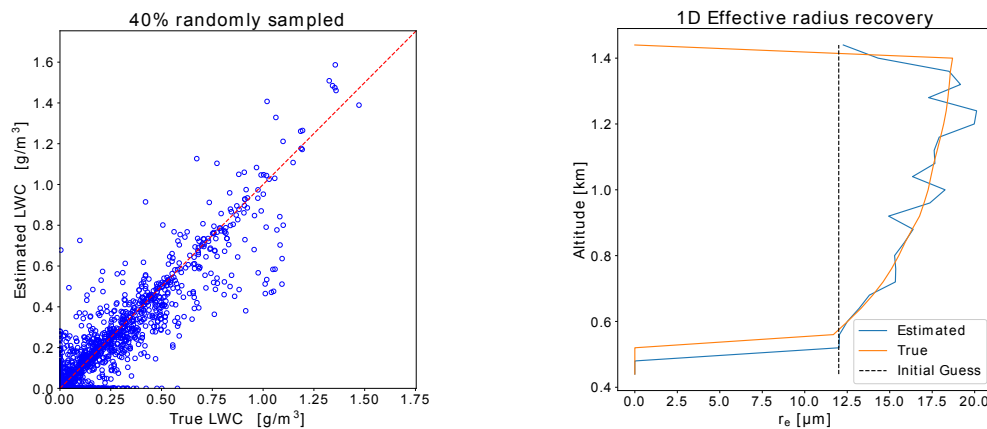


Figure 11: Scene A recovery results. [Left] Scatter plot of estimated vs. true LWC. The correlation coefficient is 0.94. [Right] recovery results of the 1D effective radius.

Figure 12: Scene A

Acknowledgements

We thank I. Koren, D. Rosenfeld, A. Aides, D. Diner, L. Di Girolamo, and G. Matheou for support and fruitful discussions. We acknowledge F. Evans and A. Doicu for the online vSHDOM code. The authors are grateful to the US-Israel Binational Science Foundation (BSF grant 2016325) for continuously facilitating our international collaboration. Aviad Levis work was partially supported by the Zuckerman Foundation. Yoav Schechner is a Landau Fellow supported by the Taub Foundation. His work was conducted in the Ollendorff Minerva Center (BMBF). Anthony Davis' work was carried out at JPL/Caltech, supported by NASA's SMD/ESD/(RST+TASNPP) and ESTO/AIST programs. Support for Jesse Loveridge's work from JPL under contract #147871 is gratefully acknowledged. This project has received funding from the European Research Council (ERC) under the European Union's Horizon 2020 research and innovation program (grant agreement No 810370: CloudCT).

References

- [1] Trenberth, K. E, Fasullo, J. T, & Kiehl, J. (2009) Earth's global energy budget. *Bulletin of the American Meteorological Society* **90**, 311–324.
- [2] Boucher, O, Randall, D, Artaxo, P, Bretherton, C, Feingold, G, Forster, P, Kerminen, V.-M, Kondo, Y, Liao, H, Lohmann, U, et al. (2013) in *Climate Change 2013: The Physical Science Basis. Contribution of Working Group I to the Fifth Assessment Report of the Intergovernmental Panel on Climate Change*. (Cambridge University Press, Cambridge (UK)), pp. 571–657.
- [3] Rosenfeld, D & Lensky, I. M. (1998) Satellite-based insights into precipitation formation processes in continental and maritime convective clouds. *Bulletin of the American Meteorological Society* **79**, 2457–2476.
- [4] Platnick, S, King, M, Ackerman, S, Menzel, W, Baum, B, Riedi, J, & Frey, R. (2003) The MODIS cloud products: Algorithms and examples from Terra. *IEEE Trans. Geosci. Remote Sens.* **41**, 459–473.
- [5] Marshak, A, Platnick, S, Várnai, T, Wen, G, & Cahalan, R. F. (2006) Impact of three-dimensional radiative effects on satellite retrievals of cloud droplet sizes. *Journal of Geophysical Research: Atmospheres* **111**.
- [6] Cho, H.-M, Zhang, Z, Meyer, K, Lebsock, M, Platnick, S, Ackerman, A. S, Di Girolamo, L, C.-Labonnote, L, Cornet, C, Riedi, J, et al. (2015) Frequency and causes of failed modis cloud property retrievals for liquid phase clouds over global oceans. *Journal of Geophysical Research: Atmospheres* **120**, 4132–4154.
- [7] National Academies of Sciences, Engineering, and Medicine. (2018) *Thriving on Our Changing Planet: A Decadal Strategy for Earth Observation from Space*. (The National Academies Press, Washington, DC, USA).
- [8] Schilling, K, Schechner, Y. Y, & Koren, I. (2019) CloudCT - computed tomography of clouds by a small satellite formation. *IAA symposium on Small Satellites for Earth Observation* pp. IAC-19-D1.6.3.
- [9] Nakajima, T & King, M. D. (1990) Determination of the optical thickness and effective particle radius of clouds from reflected solar radiation measurements. Part I: Theory. *Journal of the Atmospheric Sciences* **47**, 1878–1893.
- [10] Deschamps, P.-Y, Bréon, F.-M, Leroy, M, Podaire, A, Bricaud, A, Buriez, J.-C, & Seze, G. (1994) The POLDER mission: Instrument characteristics and scientific objectives. *IEEE Transactions on Geoscience and Remote Sensing* **32**, 598–615.
- [11] Bréon, F.-M & Goloub, P. (1998) Cloud droplet effective radius from spaceborne polarization measurements. *Geophysical Research Letters* **25**, 1879–1882.
- [12] Kalashnikova, O. V, Garay, M. J, Davis, A. B, Diner, D. J, & Martonchik, J. V. (2011) Sensitivity of multi-angle photo-polarimetry to vertical layering and mixing of absorbing aerosols: Quantifying measurement uncertainties. *Journal of Quantitative Spectroscopy and Radiative Transfer* **112**, 2149–2163.
- [13] Lukashin, C, Wielicki, B. A, Young, D. F, Thome, K, Jin, Z, & Sun, W. (2013) Uncertainty estimates for imager reference inter-calibration with CLARREO reflected solar spectrometer. *IEEE Transactions on Geoscience and Remote Sensing* **51**, 1425–1436.
- [14] Diner, D, Xu, F, Garay, M, Martonchik, J, Rheingans, B, Geier, S, Davis, A, Hancock, B, Jovanovic, V, Bull, M, et al. (2013) The Airborne Multiangle SpectroPolarimetric Imager (AirMSPI): A new tool for aerosol and cloud remote sensing. *Atmospheric Measurement Techniques* **6**, 2007–2025.
- [15] Diner, D. J, Boland, S. W, Brauer, M, Bruegge, C, Burke, K. A, Chipman, R, Di Girolamo, L, Garay, M. J, Hasheminassab, S, Hyer, E, et al. (2018) Advances in multiangle satellite remote sensing of speciated airborne particulate matter and association with adverse health effects: From MISR to MAIA. *Journal of Applied Remote Sensing* **12**, 042603.
- [16] Emde, C, Barlakas, V, Cornet, C, Evans, F, Korokin, S, Ota, Y, Labonnote, L. C, Lyapustin, A, Macke, A, Mayer, B, et al. (2015) IPRT polarized radiative transfer model intercomparison project – Phase A. *Journal of Quantitative Spectroscopy and Radiative Transfer* **164**, 8–36.
- [17] Emde, C, Barlakas, V, Cornet, C, Evans, F, Wang, Z, Labonnote, L. C, Macke, A, Mayer, B, & Wendisch, M. (2018) IPRT polarized radiative transfer model intercomparison project – three-dimensional test cases (Phase B). *Journal of Quantitative Spectroscopy and Radiative Transfer* **209**, 19–44.
- [18] Kak, A & Slaney, M. (1988) *Principles of Computerized Tomographic Imaging* IEEE Press. (IEEE Press, Piscataway, NJ, USA).
- [19] Gordon, R, Bender, R, & Herman, G. T. (1970) Algebraic reconstruction techniques (ART) for three-dimensional electron microscopy and X-ray photography. *Journal of Theoretical Biology* **29**, 471–481.
- [20] Arridge, S. R. (1999) Optical tomography in medical imaging. *Inverse Problems* **15**, R41.

- [21] Boas, D. A, Brooks, D. H, Miller, E. L, DiMarzio, C. A, Kilmer, M, Gaudette, R. J, & Zhang, Q. (2001) Imaging the body with diffuse optical tomography. *IEEE Signal Processing Magazine* **18**, 57–75.
- [22] Arridge, S. R & Schotland, J. C. (2009) Optical tomography: Forward and inverse problems. *Inverse Problems* **25**, 123010.
- [23] Che, C, Luan, F, Zhao, S, Bala, K, & Gkioulekas, I. (2018) Inverse transport networks. *arXiv preprint arXiv:1809.10820*.
- [24] Hasmonay, R. A, Yost, M. G, & Wu, C.-F. (1999) Computed tomography of air pollutants using radial scanning path-integrated optical remote sensing. *Atmos. Environ.* **33**, 267–274.
- [25] Todd, L. A, Ramanathan, M, Mottus, K, Katz, R, Dodson, A, & Mihlan, G. (2001) Measuring chemical emissions using an open-path fourier transform infrared (OP-FTIR) spectroscopy and computer-assisted tomography. *Atmos. Environ.* **35**, 1937–1947.
- [26] Kazahaya, R, Mori, T, Kazahaya, K, & Hirabayashi, J. (2008) Computed tomography reconstruction of SO₂ concentration distribution in the volcanic plume of Miyakejima, Japan, by airborne traverse technique using three UV spectrometers. *Geophys. Res. Lett.* **35**, doi:10.1029/2008GL034177.
- [27] Wright, T. E, Burton, M, Pyle, D. M, & Caltabiano, T. (2008) Scanning tomography of SO₂ distribution in a volcanic gas plume. *Geophys. Res. Lett.* **35**, doi:10.1029/2008GL034640.
- [28] Warner, J, Drake, J, & Snider, J. (1986) Liquid water distribution obtained from coplanar scanning radiometers. *Journal of Atmospheric and Oceanic Technology* **3**, 542–546.
- [29] Huang, D, Liu, Y, & Wiscombe, W. (2008) Determination of cloud liquid water distribution using 3D cloud tomography. *Journal of Geophysical Research: Atmospheres* **113**.
- [30] Huang, D, Liu, Y, & Wiscombe, W. (2008) Cloud tomography: Role of constraints and a new algorithm. *Journal of Geophysical Research: Atmospheres* **113**.
- [31] Garay, M. J, Davis, A. B, & Diner, D. J. (2016) Tomographic reconstruction of an aerosol plume using passive multiangle observations from the MISR satellite instrument. *Geophysical Research Letters* **43**, 12–590.
- [32] Diner, D. J, Beckert, J. C, Reilly, T. H, Bruegge, C. J, Conel, J. E, Kahn, R. A, Martonchik, J. V, Ackerman, T. P, Davies, R, Gerstel, S. A. W, Gordon, H. R, Muller, J.-P, Myneni, R. B, Sellers, P. J, Pinty, B, & Verstraete, M. M. (1998) Multi-angle Imaging SpectroRadiometer (MISR) instrument description and experiment overview. *IEEE Trans. Geosci. Remote Sens.* **36**, 1072–1087.
- [33] Aides, A, Schechner, Y. Y, Holodovsky, V, Garay, M. J, & Davis, A. B. (2013) Multi-sky-view 3D aerosol distribution recovery. *Optics Express* **21**, 25820–25833.
- [34] Evans, K. F. (1998) The spherical harmonics discrete ordinate method for three-dimensional atmospheric radiative transfer. *Journal of the Atmospheric Sciences* **55**, 429–446.
- [35] Doicu, A, Efremenko, D, & Trautmann, T. (2013) A multi-dimensional vector spherical harmonics discrete ordinate method for atmospheric radiative transfer. *Journal of Quantitative Spectroscopy and Radiative Transfer* **118**, 121–131.
- [36] Levis, A, Schechner, Y. Y, Aides, A, & Davis, A. B. (2015) *Airborne three-dimensional cloud tomography*. pp. 3379–3387.
- [37] Holodovsky, V, Schechner, Y. Y, Levin, A, Levis, A, & Aides, A. (2016) *In-situ multi-view multi-scattering stochastic tomography*. (IEEE), pp. 1–12.
- [38] Levis, A, Schechner, Y. Y, & Davis, A. B. (2017) *Multiple-scattering microphysics tomography*. pp. 6740–6749.
- [39] Hansen, J. E. (1971) Multiple scattering of polarized light in planetary atmospheres, Part II. Sunlight reflected by terrestrial water clouds. *Journal of the Atmospheric Sciences* **28**, 1400–1426.
- [40] Marshak, A & Davis, A. (2005) *3D Radiative Transfer in Cloudy Atmospheres*. (Springer Science & Business Media).
- [41] Chylek, P. (1978) Extinction and liquid water content of fogs and clouds. *Journal of the Atmospheric Sciences* **35**, 296–300.
- [42] Chandrasekhar, S. (1950) *Radiative Transfer*. (Oxford University Press, Oxford (UK)). [reprinted by Dover Publications, New York (NY), 1960, and by Courier Corporation, 2013].
- [43] Bohren, C. F & Huffman, D. R. (2008) *Absorption and Scattering of Light by Small Particles*. (John Wiley & Sons).
- [44] Mayer, B. (2009) *Radiative transfer in the cloudy atmosphere*. (EDP Sciences), Vol. 1, pp. 75–99.

- [45] Nakajima, T & Tanaka, M. (1988) Algorithms for radiative intensity calculations in moderately thick atmospheres using a truncation approximation. *Journal of Quantitative Spectroscopy and Radiative Transfer* **40**, 51–69.
- [46] Zhu, C, Byrd, R. H, Lu, P, & Nocedal, J. (1997) Algorithm 778: L-BFGS-B: Fortran subroutines for large-scale bound-constrained optimization. *ACM Transactions on Mathematical Software (TOMS)* **23**, 550–560.
- [47] Doicu, A & Efremenko, D. S. (2019) Linearizations of the Spherical Harmonic Discrete Ordinate Method (SHDOM). *Atmosphere* **10**, 292.
- [48] Martin, W, Cairns, B, & Bal, G. (2014) Adjoint methods for adjusting three-dimensional atmosphere and surface properties to fit multi-angle/multi-pixel polarimetric measurements. *Journal of Quantitative Spectroscopy and Radiative Transfer* **144**, 68–85.
- [49] Anderson, G. P, Clough, S. A, Kneizys, F, Chetwynd, J. H, & Shettle, E. P. (1986) AFGL atmospheric constituent profiles (0.120 km), (Air Force Geophysics Lab), Technical report.
- [50] Matheou, G & Chung, D. (2014) Large-eddy simulation of stratified turbulence. Part 2: Application of the stretched-vortex model to the atmospheric boundary layer. *Journal of the Atmospheric Sciences* **71**, 4439–4460.
- [51] Yau, M. K & Rogers, R. R. (1996) *A short course in cloud physics*. (Elsevier).
- [52] Aides, A, Schechner, Y. Y, Holodovsky, V, Garay, M. J, & Davis, A. B. (2013) Multi sky-view 3D aerosol distribution recovery. *Optics Express* **21**, 25820–25833.
- [53] Seethala, C. (2012) *Evaluating the state-of-the-art of and errors in 1D satellite cloud liquid water path retrievals with large eddy simulations and realistic radiative transfer models*.
- [54] Forster, L, Davis, A. B, Diner, D. J, & Mayer, B. (2019) Toward cloud tomography from space using MISR and MODIS: Locating the “veiled core” in opaque convective clouds. *arXiv preprint arXiv:1910.00077*.
- [55] Florescu, L, Markel, V. A, & Schotland, J. C. (2011) Inversion formulas for the broken-ray Radon transform. *Inverse Problems* **27**, 025002.
- [56] Van Harten, G, Diner, D. J, Daugherty, B. J, Rheingans, B. E, Bull, M. A, Seidel, F. C, Chipman, R. A, Cairns, B, Wasilewski, A. P, & Knobelspiesse, K. D. (2018) Calibration and validation of Airborne Multiangle SpectroPolarimetric Imager (AirMSPI) polarization measurements. *Applied Optics* **57**, 4499–4513.
- [57] Pincus, R & Evans, K. F. (2009) Computational cost and accuracy in calculating three-dimensional radiative transfer: Results for new implementations of Monte Carlo and SHDOM. *Journal of the Atmospheric Sciences* **66**, 3131–3146.
- [58] Scipy. (2020) L-BFGS-B (<https://docs.scipy.org/doc/scipy/reference/optimize.minimize-lbfgsb.html>). Accessed: 2020-01-01.
- [59] Veikherman, D, Aides, A, Schechner, Y. Y, & Levis, A. (2014) *Clouds in The Cloud*. (Springer), pp. 659–674.
- [60] Ewald, F, Zinner, T, Kölling, T, & Mayer, B. (2019) Remote sensing of cloud droplet radius profiles using solar reflectance from cloud sides – part 1: Retrieval development and characterization. *Atmospheric Measurement Techniques* **12**, 1183–1206.
- [61] Alexandrov, M. D, Cairns, B, Emde, C, Ackerman, A. S, & van Diedenhoven, B. (2012) Accuracy assessments of cloud droplet size retrievals from polarized reflectance measurements by the research scanning polarimeter. *Remote Sensing of Environment* **125**, 92 – 111.
- [62] Blyth, A. M & Latham, J. (1991) A climatological parameterization for cumulus clouds. *Journal of the Atmospheric Sciences* **48**, 2367–2371.
- [63] French, J. R, Vali, G, & Kelly, R. D. (2000) Observations of microphysics pertaining to the development of drizzle in warm, shallow cumulus clouds. *Quarterly Journal of the Royal Meteorological Society* **126**, 415–443.
- [64] Gerber, H. E, Frick, G. M, Jensen, J. B, & Hudson, J. G. (2008) Entrainment, mixing, and microphysics in trade-wind cumulus. *Journal of the Meteorological Society of Japan. Ser. II* **86**, 87–106.
- [65] Khain, P, Heiblum, R, Blahak, U, Levi, Y, Muskatel, H, Vadislavsky, E, Altaratz, O, Koren, I, Dagan, G, Shpund, J, & Khain, A. (2019) Parameterization of vertical profiles of governing microphysical parameters of shallow cumulus cloud ensembles using les with bin microphysics. *Journal of the Atmospheric Sciences* **76**, 533–560.
- [66] Pinsky, M & Khain, A. (2018) Theoretical analysis of the entrainment–mixing process at cloud boundaries. part I: Droplet size distributions and humidity within the interface zone. *Journal of the Atmospheric Sciences* **75**, 2049–2064.
- [67] Bera, S, Prabha, T. V, & Grabowski, W. W. (2016) Observations of monsoon convective cloud microphysics over india and role of entrainment-mixing. *Journal of Geophysical Research: Atmospheres* **121**, 9767–9788.

- [68] Costa, A. A, de Oliveira, C. J, de Oliveira, J. C. P, & da Costa Sampaio, A. J. (2000) Microphysical observations of warm cumulus clouds in ceara, brazil. *Atmospheric Research* **54**, 167–199.
- [69] Lu, M.-L, Feingold, G, Jonsson, H. H, Chuang, P. Y, Gates, H, Flagan, R. C, & Seinfeld, J. H. (2008) Aerosol-cloud relationships in continental shallow cumulus. *Journal of Geophysical Research: Atmospheres* **113**.
- [70] Martins, J. A & Dias, M. A. F. S. (2009) The impact of smoke from forest fires on the spectral dispersion of cloud droplet size distributions in the amazonian region. *Environmental Research Letters* **4**, 015002.
- [71] Hudson, J. G, Noble, S, & Jha, V. (2012) Cloud droplet spectral width relationship to ccn spectra and vertical velocity. *Journal of Geophysical Research: Atmospheres* **117**.
- [72] Pandithurai, G, Dipu, S, Prabha, T. V, Mahes Kumar, R. S, Kulkarni, J. R, & Goswami, B. N. (2012) Aerosol effect on droplet spectral dispersion in warm continental cumuli. *Journal of Geophysical Research: Atmospheres* **117**.
- [73] Igel, A. L & van den Heever, S. C. (2017) The importance of the shape of cloud droplet size distributions in shallow cumulus clouds. part I: Bin microphysics simulations. *Journal of the Atmospheric Sciences* **74**, 249–258.
- [74] Lu, M.-L & Seinfeld, J. H. (2006) Effect of aerosol number concentration on cloud droplet dispersion: A large-eddy simulation study and implications for aerosol indirect forcing. *Journal of Geophysical Research: Atmospheres* **111**, D02207.
- [75] Wang, X, Xue, H, Fang, W, & Zheng, G. (2011) A study of shallow cumulus cloud droplet dispersion by large eddy simulations. *Acta Meteorologica Sinica* **25**, 166–175.
- [76] Milbrandt, J. A & Yau, M. K. (2005) A multimoment bulk microphysics parameterization. part I: Analysis of the role of the spectral shape parameter. *Journal of the Atmospheric Sciences* **62**, 3051–3064.
- [77] Cairns, B, Russell, E. E, & Travis, L. D. (1999) *Research Scanning Polarimeter: Calibration and ground-based measurements*,. (International Society for Optics and Photonics), Vol. 3754, pp. 186–196.

Appendix

A Jacobian Derivation

In Eq. [44] of the main text, the Jacobian is written as a sum of six terms

$$\partial_g \mathbf{I}[k] = A_1 + A_2 + A_3 + A_4 + A_5 + A_6. \quad (50)$$

In this section we expand and describe each of these terms. Using Eqs. [16] and [28], the transmittance derivative is

$$\partial_g T(\mathbf{x}_1 \rightarrow \mathbf{x}_2) = -T(\mathbf{x}_1 \rightarrow \mathbf{x}_2) \ell_g(\mathbf{x}_1 \rightarrow \mathbf{x}_2) \partial_g \beta. \quad (51)$$

Then,

$$A_1 = -\ell_g(\mathbf{x}_0 \rightarrow \mathbf{x}_k) \mathbf{I}(\mathbf{x}_0, \boldsymbol{\omega}_k) T(\mathbf{x}_0 \rightarrow \mathbf{x}_k) [\partial_g \beta], \quad (52)$$

$$A_2 = \ell_g(\mathbf{x}_0 \rightarrow \mathbf{x}_k) \int_{\mathbf{x}_0}^{\mathbf{x}_k} \left[\frac{\partial_g \varpi}{4\pi} \int_{4\pi} \mathbf{P}(\mathbf{x}', \boldsymbol{\omega}_k \cdot \boldsymbol{\omega}') \mathbf{I}(\mathbf{x}', \boldsymbol{\omega}') d\boldsymbol{\omega}' \right] \beta(\mathbf{x}') T(\mathbf{x}' \rightarrow \mathbf{x}_k) d\mathbf{x}', \quad (53)$$

$$A_3 = \ell_g(\mathbf{x}_0 \rightarrow \mathbf{x}_k) \int_{\mathbf{x}_0}^{\mathbf{x}_k} \left\{ \frac{\varpi(\mathbf{x}')}{4\pi} \int_{4\pi} [\partial_g \mathbf{P}(\mathbf{x}', \boldsymbol{\omega}_k \cdot \boldsymbol{\omega}')] \mathbf{I}(\mathbf{x}', \boldsymbol{\omega}') d\boldsymbol{\omega}' \right\} \beta(\mathbf{x}') T(\mathbf{x}' \rightarrow \mathbf{x}_k) d\mathbf{x}', \quad (54)$$

$$A_4 = \int_{\mathbf{x}_0}^{\mathbf{x}_k} \left\{ \frac{\varpi(\mathbf{x}')}{4\pi} \int_{4\pi} \mathbf{P}(\mathbf{x}', \boldsymbol{\omega}_k \cdot \boldsymbol{\omega}') [\partial_g \mathbf{I}(\mathbf{x}', \boldsymbol{\omega}')] d\boldsymbol{\omega}' \right\} \beta(\mathbf{x}') T(\mathbf{x}' \rightarrow \mathbf{x}_k) d\mathbf{x}', \quad (55)$$

$$A_5 = \ell_g(\mathbf{x}_0 \rightarrow \mathbf{x}_k) [\partial_g \beta] \int_{\mathbf{x}_0}^{\mathbf{x}_k} \mathbf{J}(\mathbf{x}', \boldsymbol{\omega}_k) T(\mathbf{x}' \rightarrow \mathbf{x}_k) d\mathbf{x}', \quad (56)$$

$$A_6 = -\ell_g(\mathbf{x}_0 \rightarrow \mathbf{x}_k) [\partial_g \beta] \int_{\mathbf{x}_0}^{\mathbf{x}_k} \mathbf{J}(\mathbf{x}', \boldsymbol{\omega}_k) \beta(\mathbf{x}') T(\mathbf{x}' \rightarrow \mathbf{x}_k) d\mathbf{x}'. \quad (57)$$

Note that $\mathbf{I}(\mathbf{x}, \boldsymbol{\omega})$ and $\mathbf{J}(\mathbf{x}, \boldsymbol{\omega})$ are computed in Step 1 and are therefore ready for use when computing A_1, A_2, A_3, A_5 and A_6 . Furthermore, $\ell_g(\mathbf{x}_0 \rightarrow \mathbf{x}_k) = 0$ for any voxel that is not on the LOS of pixel k . Therefore, the terms A_1, A_2, A_3, A_5, A_6 are computed using a single path tracing $\mathbf{x}_k \rightarrow \mathbf{x}_0$.

We now give special attention to A_4 in Eq. [55]. Using the diffuse-direct decomposition of (21), we decompose (55) as

$$\begin{aligned} A_4 &= \int_{\mathbf{x}_0}^{\mathbf{x}_k} \left\{ \frac{\varpi(\mathbf{x}')}{4\pi} \int_{4\pi} \mathbf{P}(\mathbf{x}', \boldsymbol{\omega}_k \cdot \boldsymbol{\omega}') [\partial_g \mathbf{I}_d(\mathbf{x}', \boldsymbol{\omega}')] d\boldsymbol{\omega}' \right\} \beta(\mathbf{x}') T(\mathbf{x}' \rightarrow \mathbf{x}_k) d\mathbf{x}' \\ &+ \int_{\mathbf{x}_0}^{\mathbf{x}_k} \left\{ \frac{\varpi(\mathbf{x}')}{4\pi} \int_{4\pi} \mathbf{P}(\mathbf{x}', \boldsymbol{\omega}_k \cdot \boldsymbol{\omega}') \delta(\boldsymbol{\omega}' - \boldsymbol{\omega}_{\text{Sun}}) \mathbf{F}_{\text{Sun}} [\partial_g T(\mathbf{x}_{\text{Sun}} \rightarrow \mathbf{x}')] d\boldsymbol{\omega}' \right\} \beta(\mathbf{x}') T(\mathbf{x}' \rightarrow \mathbf{x}_k) d\mathbf{x}'. \end{aligned} \quad (58)$$

The first term in (58) is based on $\partial_g \mathbf{I}_d$, i.e., a derivative of the diffuse (high order scattering) component. Herein lies a recursive complexity. In principle, a differential change in the microphysics of one voxel can recursively affect the radiance at every other voxel, and this affects all the pixels. To make calculations numerically efficient, we approximate (58). The approximation assumes that relative to other components in the Jacobian, \mathbf{I}_d is less sensitive to a differential changes in the microphysical properties at voxel g . Thus, (58) is approximated by keeping \mathbf{I}_d independent of Θ for a single iteration of the gradient computation, i.e.,

$$\partial_g \mathbf{I}_d \approx 0. \quad (59)$$

The second term in (58) is based on differentiation of the direct component. This is straight-forward to compute using (51). Consequently, using Eq. [59] and the definition of $\mathbf{I}_{\text{Single}}(\mathbf{x}_{\text{Sun}} \rightarrow \mathbf{x}' \rightarrow \mathbf{x}_k)$ in (25), the term A_4 in (58) is approximated by

$$A_4 \approx \tilde{A}_4 = [\partial_g \beta] \int_{\mathbf{x}_0}^{\mathbf{x}_k} \ell_g(\mathbf{x}_{\text{Sun}} \rightarrow \mathbf{x}') \mathbf{I}_{\text{Single}}(\mathbf{x}_{\text{Sun}} \rightarrow \mathbf{x}' \rightarrow \mathbf{x}_k) d\mathbf{x}'. \quad (60)$$

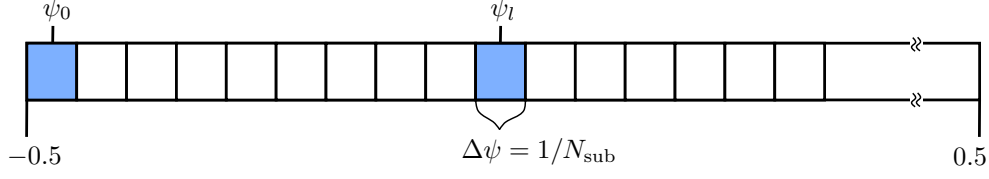


Figure 13: A normalized frame spans the interval $[-0.5, 0.5]$, evenly divided into N_{sub} subframes.

Table 1: Modulation parameters [56] used for synthesis of AirMSPI measurements.

$\gamma_0(470\text{nm})$	$\gamma_0(660\text{nm})$	$\gamma_0(865\text{nm})$	$\xi(470\text{nm})$	$\xi(660\text{nm})$	$\xi(865\text{nm})$	η
4.472	3.081	2.284	1.0	0.27	0.03	0.009

The term $\ell_g(\mathbf{x}_{\text{Sun}} \rightarrow \mathbf{x}')$ in (60) contributes to voxels *outside* of the LOS. The integral in \tilde{A}_4 is computed with a *broken-ray* [55] path $\mathbf{x}_k \rightarrow \mathbf{x}' \rightarrow \mathbf{x}_{\text{Sun}}$, as illustrated in Fig. 4.

Using Eqs. [17,51,52,57], A_1 and A_6 are combined to

$$A_{1,6} = A_1 + A_6 = -[\partial_g \beta] \mathbf{I}(\mathbf{x}_g, \boldsymbol{\omega}_k). \quad (61)$$

Overall, in our iterative procedure, we approximate the Jacobian in (44) by

$$\partial_g \mathbf{I}[k] = A_{1,6} + A_2 + A_3 + \tilde{A}_4 + A_5. \quad (62)$$

Equations [52]–[60] formulate the Jacobian in terms of a voxel grid (zero-order interpolation). However, in practice we use a trilinear interpolation kernel K in (27), consistent with vSHDOM internal interpolation [34].

B Measurement Noise

The inverse problem defined in the main text is formulated in terms of measured Stokes vectors [Eq. 30]. However, Stokes vectors are not measured directly. Rather, they are derived from intensity measurements taken through filters. The raw intensity measurements are noisy. Noise is dominated by Poisson photon noise, which is independent across different raw measurements. However, the estimation of Stokes components *from* independent intensity measurements yields noise which is correlated across the components of the Stokes vector, per-pixel. In this section, we describe the synthesis model we employ to generate realistic noise in simulations. Our synthesis is based on the AirMSPI [56] sensor model. Furthermore, we derive the expression for \mathbf{R} , which we use in the recovery process (Eq. [36] in the main text).

AirMSPI measures a modulated intensity signal at $N_{\text{sub}}=23$ subframes. Define a normalized frame which spans the unitless integration time interval $\psi \in [-0.5, 0.5]$. Denote the temporal center and span of each subframe as ψ_l and $\Delta\psi = 1/N_{\text{sub}}$, respectively (Fig. 13). Based on the sensing process described in Ref. [56], define the following modulation function, whose parameters are given in Table 1:

$$M[l] = J_0[\kappa(\psi_l)] + \frac{1}{3} \left(\frac{\pi \Delta\psi}{2} \right)^2 \gamma_0^2(\lambda) \left\{ J_2[\kappa(\psi_l)] - \cos[2(\pi\psi_l - \eta)] J_0[\kappa(\psi_l)] \right\}, \quad (63)$$

with

$$\kappa(\psi_l) = -2\gamma_0(\lambda) \sin(\pi\psi_l - \eta) \sqrt{1 + \cot^2(\pi\psi_l - \eta)}. \quad (64)$$

Here J_0 , J_2 are the Bessel functions of the first kind of order 0 and 2, respectively. Denote by $\xi(\lambda)$ a wavelength-dependent ratio, which is drawn from quantum efficiencies and spectral bandwidths⁶ of each AirMSPI band (Table 1). Using simulated Stokes vectors derived by vSHDOM, AirMSPI measurements are synthesised as passing through two polarization analyzing filters [56]. As defined in Eq. [20] in the main text, $\mathbf{I}[k]$ is the Stokes vector in pixel k . Correspondingly the intensity is $I[k]$, while $Q[k]$, $U[k]$ are the polarized components. Measurements l through the two filters of AirMSPI are modeled by

$$d_0[l, k] = \xi(\lambda)(I[k] + M[l]Q[k]) \quad (65)$$

$$d_{45}[l, k] = \xi(\lambda)(I[k] + M[l]U[k]), \quad (66)$$

⁶For the exact calculation of the ratio see Eq. [24] of [56].

vSHDOM			L-BFGS		
N_μ	N_ϕ	splitting accuracy	gtol	gtol	maxls
8	16	0.1	$1e^{-16}$	$1e^{-16}$	30

Table 2: Numerical parameters. For vSHDOM parameter definitions, see Ref. [57]. For L-BFGS parameter definitions, see Ref. [58].

where $M[l]$ and $\xi(\lambda)$ are given in Eq. [63] and Table 1, respectively. The units of d are Watts. Define $\mathbf{d}[k] = (d_0[1, k], \dots, d_0[N_{\text{sub}}, k], d_{45}[1, k], \dots, d_{45}[N_{\text{sub}}, k])^\top$. In matrix form, the transformations by Eqs. [65-66] are written using a single 46×3 modulation matrix \mathbf{M}

$$\mathbf{d}[k] = \mathbf{M}\mathbf{I}[k]. \quad (67)$$

Detection is by a camera which generates photo-electrons in each pixel well. The relation between $d_0[l, k]$ or $d_{45}[l, k]$ and the *expected* unit-less number of photo-electrons in the pixel is given by a gain G . The number of photo-electrons is random (*Poissonian*) around this expected value. The vector of simulated electron counts is thus synthesized by a Poisson process

$$\mathbf{e}[k] \sim \text{Poisson}\left\{\text{round}(G \cdot \mathbf{d}[k])\right\} = \text{Poisson}\left\{\text{round}(G \cdot \mathbf{M}\mathbf{I}[k])\right\}. \quad (68)$$

The gain G is chosen to let the maximum signal at each camera view (i.e. maximum over pixels, wavelengths and subframe measurements) reach the maximum *full-well depth* of 200,000 electrons, consistent with AirMSPI specifications. (68) synthesizes raw AirMSPI signals including noise (Fig. 8). The synthesized AirMSPI signals, including this noise, are now used as inputs to the calculation of measured Stokes vectors in each pixel and viewpoint. The vector of electron counts $\mathbf{e}[k]$ in each pixel k is transformed into Stokes synthetic data [Eq. 30] using a 3×46 demodulation matrix \mathbf{W}

$$\mathbf{y}_\mathbf{I}[k] = (\mathbf{M}^\top \mathbf{M})^{-1} \mathbf{M}^\top \mathbf{e}[k] = \mathbf{W}\mathbf{e}[k]. \quad (69)$$

The vectors $\mathbf{y}_\mathbf{I}[k]$ form the data for tomographic analysis.

Our tomographic analysis takes into account the noise properties, including noise correlation. As we now show, the measurement model [69] yields correlated noise of different Stokes components. Thus, \mathbf{R}^{-1} ((36)) is not diagonal. Denote the diagonal co-variance matrix of the photo-electron readings by $\mathbf{C}_e^{-1} = \text{diag}(\mathbf{e})$. Let $\mathcal{I}_{46 \times 46}$ denote the *Identity* matrix. The signal is generally dominated by unpolarized multiply-scattered background light. Relative to it, the magnitude of the modulated polarization signal is small. Thus, per pixel k , the diagonal matrix $\mathbf{C}_e^{-1}[k]$ is approximately constant with a global weight

$$\mathbf{C}_e^{-1}[k] \approx \alpha[k] \mathcal{I}_{46 \times 46}. \quad (70)$$

Using Eqs. [69,70] for each pixel, the Stokes co-variance matrix is

$$\mathbf{C}^{-1}[k] = \mathbf{M}^\top \mathbf{C}_e^{-1}[k] \mathbf{M} \approx \alpha[k] \mathbf{M}^\top \mathbf{M}. \quad (71)$$

A maximum-likelihood estimator corresponding to a Poisson process should have a weight $\alpha[k] \propto 1/\|\mathbf{e}\|_1$, to account for higher photon noise in brighter pixels. In simulations, however, we found that $\alpha[k] = 1$ worked better. This is perhaps due to richer information carried by denser cloud regions, i.e. brighter pixels. Overall the expression we minimize in (36) is

$$\hat{\Theta} = \arg \min_{\Theta} \sum_{k=1}^{N_{\text{meas}}} (\mathbf{I}[k] - \mathbf{y}_\mathbf{I}[k])^\top \mathbf{M}^\top \mathbf{M} (\mathbf{I}[k] - \mathbf{y}_\mathbf{I}[k]), \quad (72)$$

i.e. $\mathbf{R}^{-1} = \mathbf{M}^\top \mathbf{M}$.

C Numerical considerations

In this section we describe numerical considerations that stabilize the recovery.

C.1 Hyper-parameters

Our code requires the choice of hyper-parameters for rendering with vSHDOM [57] in Step 1 and optimization with *scipy* L-BFGS [46, 58] in Step 2. Table 2 summarizes the numerical parameters used in our simulations.

C.2 Preconditioning

Multivariate optimization can suffer from ill-conditioning due to different scales of the sought variables. This is expected when recovered variables represent different physical quantities with different units and orders of magnitude. A preconditioning of the update rule in (38) takes the following form

$$\Theta_{b+1} = \Theta_b - \chi_b \mathbf{\Pi}^{-1} \nabla_{\Theta} \mathcal{D}(\mathbf{I}_{\Theta}, \mathbf{y}), \quad (73)$$

where we apply a diagonal scaling matrix $\mathbf{\Pi}$ (*Jacobi* preconditioner) to scale the different physical variables (LWC, r_e). Thus, $\mathbf{\Pi}$ takes the form

$$\mathbf{\Pi} = \text{diag}(\Pi_{\text{LWC}}, \Pi_{r_e}, \dots, \Pi_{\text{LWC}}, \Pi_{r_e}). \quad (74)$$

In our tests, we use $\Pi_{\text{LWC}} = 15$ and $\Pi_{r_e} = 0.01$ to scale the parameters to a similar magnitude and closer to unity upon initialization.

C.3 Initialization

The recovery is initialized by the estimation of a cloud voxel mask, which bounds the cloud 3D shape. The 3D shape bound of the cloud is estimated using *Space-Carving* [59]. Space-carving is a geometric approach to estimate a bound to 3D shape via multi-view images. The following steps are performed in our space-carving algorithm

1. Each image is segmented into *potentially cloudy* and *non-cloudy* pixels (we use a simple radiance threshold).
2. From each camera viewpoint, each *potentially cloudy* pixel back-projects a ray into the 3D domain. Voxels that this ray crosses are voted as potentially cloudy.
3. Voxels which accumulate “cloudy” votes in at least 8 out of the 9 AirMSPI viewpoints are marked as cloudy.

Outside of the shape bound, LWC = 0 throughout iterations. Within the estimated cloud-shape bound, the volume content is initialized as homogeneous with LWC = 0.01 g/m³, $r_e = 12\mu\text{m}$ and $v_e = 0.1$. Then, inside of the shape-bound, $\{\text{LWC}, r_e, v_e\}$ change throughout iterations, possibly diminishing LWC to very small values.

C.4 Convergence

Our approach alternates between Step 1 (RTE rendering) and Step 2 (approximate gradient) until convergence (Fig. 7). The convergence criteria are dictated by the L-BFGS step: at each iteration, the relative change to the forward model and its gradient are compared to the *ftol* and *gtol* parameters (see Table 2 for values used). See *SciPy* documentation [58] for exact description of the L-BFGS stopping criteria.

D Qualitative Results: Scene B

Qualitative volumetric results of the recovered LWC for Scene B are shown in Fig. 14. A scatter plot of the recovered LWC and the recovery results of r_e for Scene B are given in Fig. 15.

E Spatial Variation of The Effective Radius

In nature, generally the droplet effective radius r_e and variance v_e vary in 3D. However, operational remote sensing algorithms, which rely on 1D RT and plane-parallel cloud models, retrieve a single value for r_e (and for v_e), for each cloudy pixel. This occurs both in bi-spectral [9, 60] and polarimetric [11, 61] techniques. In these approaches, it is always uncertain which portion of the cloud the retrieved quantity corresponds to, because light penetrates into the cloud and simultaneously scatters from different depths inside it. In polarization analysis of plane-parallel cloud models, it is often assumed that the retrieved microphysical parameters correspond approximately to an optical depth of unity. At any rate, this uncertainty complicates the interpretation of retrieved values in studies which rely on them.

The mathematical approach of the paper is formulated for 3D variation of all the required fields: LWC, r_e , v_e . As Fig. 3 in the main paper shows, polarization is sensitive to r_e of any voxel which scatters sunlight towards the camera. Moreover, the formulation explicitly models and seeks spatially varying microphysics, using multi-angular data. We confidently anticipate the same sensitivity to v_e . The demonstrations in the simulations used a representation in which r_e varies vertically, not horizontally. This is more general than the operational methods mentioned above, yet more degenerate than full 3D heterogeneity. We now discuss the implication of such a representation.

Textbook cloud physics (e.g., [51]) is based on the mental picture of a parcel of moist air containing a certain number of cloud condensation nuclei that is ascending vertically in the buoyancy-driven part of the convective cycle. Since

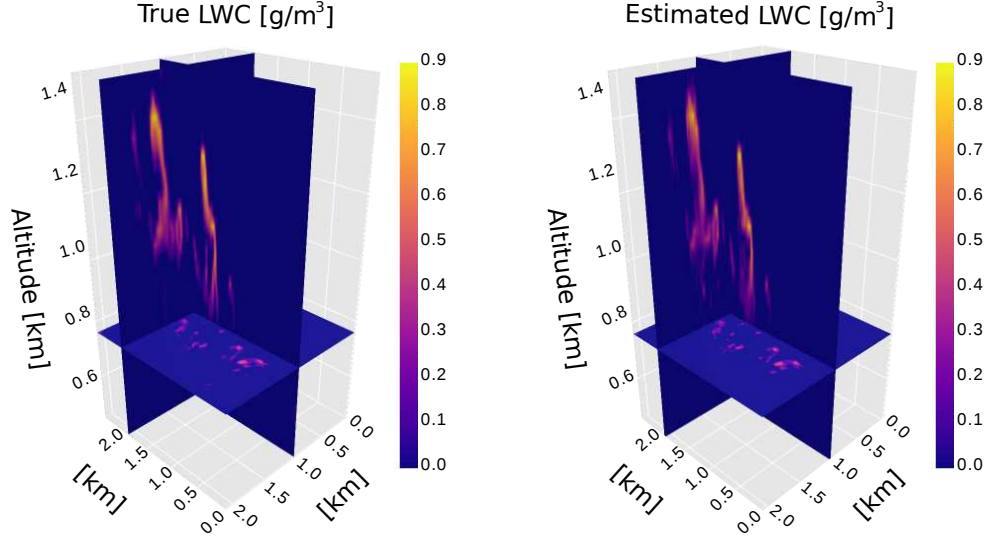


Figure 14: Scene B recovery results. [Left] Slices of the true LES generated region. [Right] Slices of the estimated region.

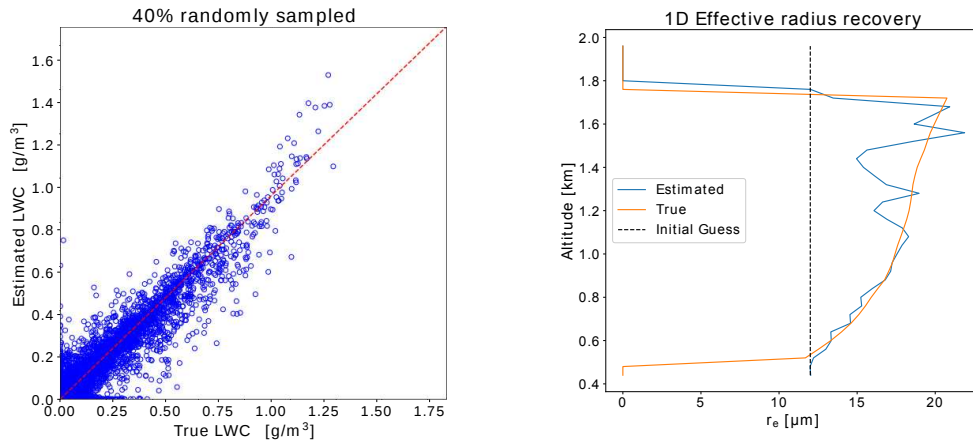


Figure 15: Scene B [Left] Scatter plot of the estimated vs. true LWC. The fit correlation is 0.96. [Right] Recovery results of the 1D effective radius

temperature and pressure are strongly stratified environmental quantities, moist adiabatic thermodynamics thus predict a vertically-varying droplet size distribution, at least in the so-called “convective core” of the cloud. For the present study, this restriction of microphysical variability to the vertical dimension only applies to both r_e and v_e .

There is compelling evidence that the horizontal variability r_e is indeed small over a cloud scale. This evidence comes from in-situ aircraft observations of shallow cumulus [62, 63, 64], modelling studies [65] and theory [66]. However, there are also select observations of monsoonal clouds [67] and theoretical arguments [66] that suggest there is a sharp gradient in the droplet effective radius in the very outer shell of the clouds. If this is the case, then a representation having vertical-only variation of r_e loses validity at the outer shell. This may cause bias in retrievals based on polarimetry. The reason is that polarization signals are dominated by single-scattering, which is most likely to occur at shallow depth in the cloud.

The value of v_e can also vary significantly across different environmental conditions. This is seen in research flights including in-situ measurements [68, 69, 70, 71, 72]. Moreover, in LES simulations of shallow cumulus clouds with bin microphysics, v_e might range from 0.01 to 0.26 [73]. The core of a cloud tends to have a low effective variance as condensation is the dominant process there [74, 73]. Cloud edges, in contrast, experience also evaporation and entrainment mixing, as the cloud is diluted by environmental air [75]. This tends to increase v_e . If the cloud has precipitation, spatial variability of v_e increases [76].

These points show that, on the one hand, the approximations in the demonstrations are often reasonable. On the other hand, it is indeed worth representing cloud microphysical parameters as functions in 3D, then retrieving them in tomography, to push the frontier of cloud physics research. Retrieving a large number of degrees of freedom can be managed better by using more information from diverse sources. One option is to include additional sources of measurements, e.g., by using a combination of the AirMSPI [14] and Research Spectro-Polarimeter (RSP) [77] airborne instruments. Another option is to introduce tailored regularization schemes, which mathematically express the natural trends of horizontal variability mentioned above. The 3D tomographic approach presented in the paper is a significant enabler for probing such questions. It offers more flexibility than current operational analyses, which are largely based on 1D RT and bulk retrieved values for a whole cloud.